

Partitioning statistics of a correlated few-electron droplet

Jashwanth Shaju,^{1,*} Elina Pavlovska,^{2,*} Ralfs Suba,² Junliang Wang,¹
 Seddik Ouacel,¹ Thomas Vasselon,¹ Matteo Aluffi,¹ Lucas Mazzella,¹ Clement
 Geffroy,¹ Arne Ludwig,³ Andreas D. Wieck,³ Matias Urdampileta,¹
 Christopher Bäuerle,¹ Vyacheslavs Kashcheyevs,^{2,†} and Hermann Sellier^{1,‡}

¹*Université Grenoble Alpes, CNRS, Grenoble INP,
 Institut Néel, F-38000 Grenoble, France*

²*Department of Physics, University of Latvia, Riga, LV-1004, Latvia*

³*Lehrstuhl für Angewandte Festkörperphysik, Ruhr-Universität Bochum,
 Universitätsstraße 150, D-44780 Bochum, Germany*

(Dated: August 27, 2024)

Emergence of universal collective behaviour from interactions in a sufficiently large group of elementary constituents is a fundamental scientific paradigm [1]. In physics, correlations in fluctuating microscopic observables can provide key information about collective states of matter such as deconfined quark-gluon plasma in heavy-ion collisions [2] or expanding quantum degenerate gases [3, 4]. Two-particle correlations in mesoscopic colliders have provided smoking-gun evidence on the nature of exotic electronic excitations such as fractional charges [5, 6], levitons [7] and anyon statistics [8]. Yet the gap between two-particle collisions and the emergence of collectivity [9] as the number of interacting particles grows [10] is hard to address at the microscopic level. Here, we demonstrate all-body correlations in the partitioning of up to $N = 5$ electron droplets driven by a moving potential well through a Y-junction in a semiconductor. We show that the measured multivariate cumulants (of order $k = 2 \dots N$) of the electron droplet are accurately described by k -spin correlation functions of an effective Ising model below the Néel temperature and can be interpreted as a Coulomb liquid in the thermodynamic limit. Finite size scaling of high-order correlation functions provides otherwise inaccessible fingerprints of emerging order. Our demonstration of emergence in a simple correlated electron collider opens a new way to study engineered states of matter.

* These authors contributed equally to this work.

† corresponding author: slava@latnet.lv

‡ corresponding author: hermann.sellier@neel.cnrs.fr

INTRODUCTION

Breaking-up matter into pieces and studying the statistics of fragments is one of the basic epistemic strategies in physics. Arguably the most exquisite pursuit of this strategy is the success of high-energy particle colliders in discovering and quantifying the fundamental types of matter within the Standard Model of elementary particles. The quantum chromodynamics (QCD) sector of the latter is particularly challenging as the fundamental particles of QCD — quarks and gluons — at low energies condense into strongly correlated “droplets” (hadrons) due to the phenomenon of color confinement. A deconfinement phase transition from a liquid of hadrons into quark-gluon plasma [11] has been extensively studied in relativistic heavy ion collisions where pairs of colliding nuclei create a fireball of high baryonic density and temperature. In particular, measurements of high-order cumulants in the number of particles produced as the fireball quenches (collision multiplicity) [12] can be used [2] to pinpoint the critical point in the QCD phase diagram [13, 14]. Fluctuations in multiplicity and correlations of the detected transverse momenta carry rich information about the collective dynamics of QCD matter that continues to be a vibrant area of research at the interface of heavy-ion and high-energy physics [9]. In solid-state nanoelectronic circuits, charged quasi-particles can be guided with on-demand single electron sources to a small interaction area such as a quantum point contact [7, 15] or an energy barrier [16–18], creating a collider analogue for electronic matter. Second order correlations in steady-state and on-demand collisions have provided an essential signal to decode partitioning noise of composite particles [5, 6], fermionic [7, 15] and anyonic exchange statistics [8] and two-particle Coulomb interactions [16–18]. In previous research, temporal electronic correlations in nanostructures have been extensively studied [19–24]. These experiments primarily investigate the Coulomb interaction between two adjacent electrons as they traverse a quantum point contact, quantum dot, or tunnel junction. Higher-order ($k > 2$) correlations in current fluctuations [25, 26] and electron counting statistics [22, 27, 28] have been recognised as important signatures of Coulomb interactions, yet evidence for the corresponding collective behaviour in on-chip transport has been difficult to interpret [29] due to limited control over the number of particles interacting and the dominating randomness of tunneling times. In the thermodynamic limit, Coulomb interactions in a two-dimensional electron gas (2DEG) lead to a rich phase diagram as function of the electron density, temperature and magnetic field, including strongly correlated Coulomb liquid, Wigner crystals and quantum Hall phases [30].

ON-CHIP MULTI-ELECTRON COLLIDER

Here we address emergence of correlated states of electronic matter by studying high-order correlations in controlled multi-electron collisions. This is done by implementing a Y-junction in a GaAs semiconductor heterostructure to investigate the partitioning of a charge droplet of interacting electrons within a highly controlled environment as illustrated in Fig. 1. Two single-electron sources and two single-shot detectors are made of gate-defined quantum dots (QD) paired with nearby quantum point contacts (QPC) used as charge sensors. By recording the discrete jumps in the QPC current I_{QPC} , the precise electron number within the QD is measured. Several pairs of parallel electrodes define depleted 1D transport channels, guiding the electron droplet from the source to the detectors. The 40 μm -long central channel includes a narrow 30 nm-wide barrier gate that enables precise tuning of the electron droplet partitioning. At the end of the channel, a Y-junction splits the electron droplet in two and directs the “reaction products” into the detectors.

The electron droplet is transported in a highly controlled way within a single piezoelectric

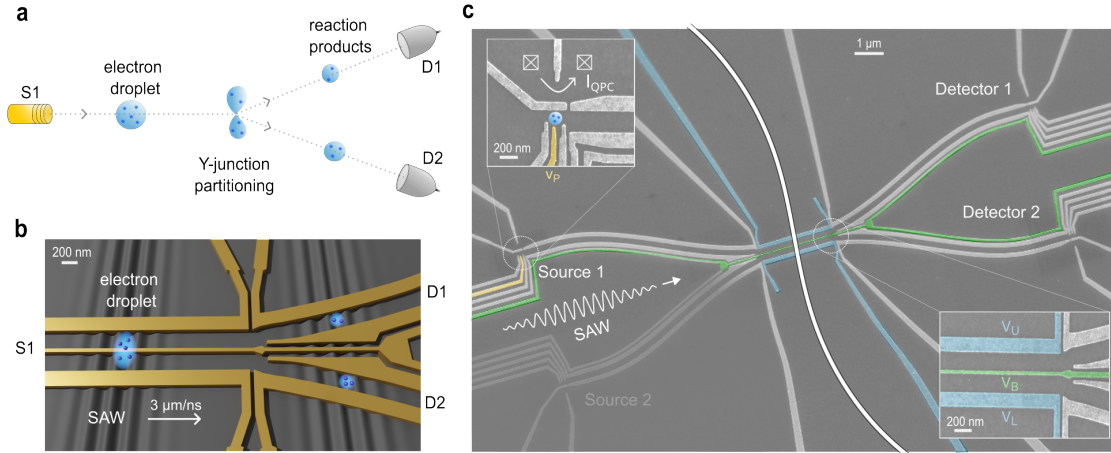


Fig. 1. **Partitioning of an electron droplet.** **a**, Schematic of the experiment. An electron source (S1) delivers a few-electron droplet which is split in-flight at a Y-junction. The output of the partitioning is analysed by two single-shot detectors (D1 and D2). **b**, Schematic of the electron droplet transport inside the selected potential minimum of a surface acoustic wave (SAW). Electrostatic gates (yellow) are used to guide the electron droplet and create a Y-junction. **c**, Scanning electron microscope image of the device showing the metallic surface gates (light grey). The electron source (S1) consists of a quantum dot (shown in the top left inset) coupled to a quantum point contact (QPC) for charge sensing. The plunger gate (yellow) is employed to inject a precise number of electrons into a single SAW minimum. A second electron source (S2) is connected to the central channel for control experiments and to inject more electrons. The Y-junction at the end of the central channel (see bottom inset) enables partitioning of the electron droplet.

potential minimum of a surface acoustic wave (SAW) [31–33]. An interdigital transducer, positioned 1.5 mm away, generates a 180 μm -long SAW train. By applying a voltage pulse v_P on the plunger gate, which is significantly shorter in duration than the SAW period, a well-defined number of electrons (ranging from 1 to 5) can be loaded into a single SAW minimum. These electrons remain confined in the moving quantum dot [34], which then shuttles them along the rails to the detectors. Loading more than 3 electrons simultaneously into a single SAW minimum from a single source is technically very challenging. To address this, we employ a technique where we load electrons from two sources and synchronise them. Because the channel is 40 μm long, electrons lose their history and become statistically indistinguishable (see Supplementary Note 2).

PARTITIONING OF AN ELECTRON DROPLET

To explore electron interactions within the droplet, we analyse partitioning data for up to five electrons. Fig. 2 presents an example with $N = 4$ electrons, while the other cases are shown in Extended Data Fig. 1 and 2. The counting statistics is represented by the probabilities $P_{(N-n, n)}$, where $N - n$ and n are the numbers of electrons detected in D2 and D1, respectively.

The simplest case is when the 4 electrons are placed in different SAW minima (Fig. 2a) such that they do not form a droplet and cannot interact. We find that the counting statistics $P_{(N-n, n)}$ can be reconstructed from single-electron partitioning data (solid lines) and thus

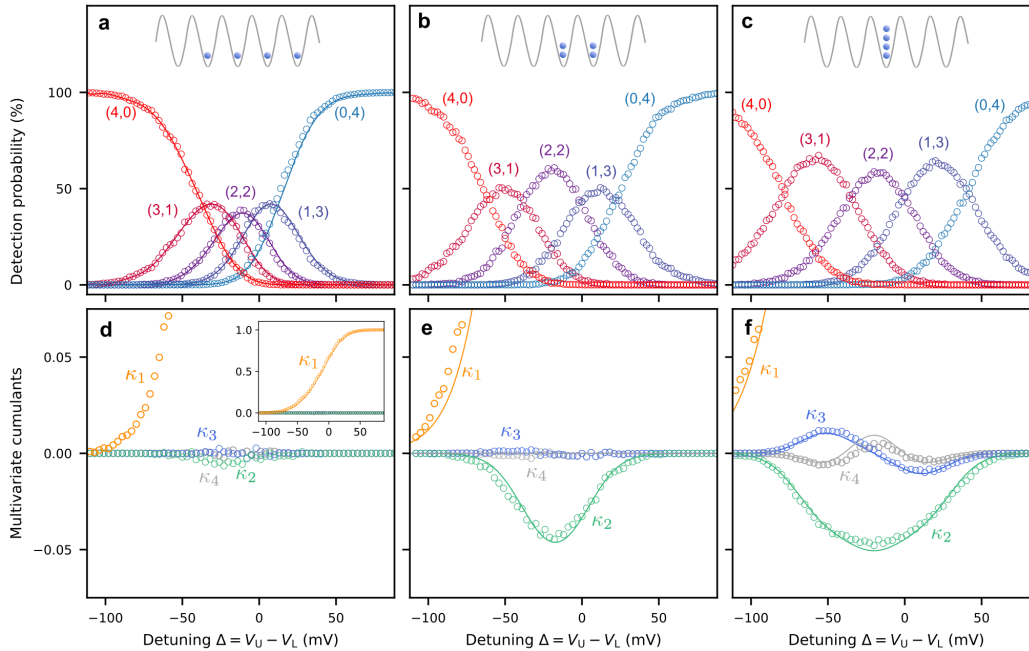


Fig. 2. **Partitioning of an electron droplet containing $N = 4$ electrons.** **a-c**, Detection probabilities $P_{(N-n, n)}$ versus side-gate detuning voltage Δ . Each data point is extracted from 3000 single-shot measurements. The labels $(N - n, n)$ correspond to the events where n electrons are measured at detector D1 and $N - n$ electrons at detector D2. In **a**, the four electrons are distributed across different SAW minima, as illustrated in the top inset. In **b**, the four electrons are loaded into adjacent minima, with two electrons in each. In **c**, all four electrons are confined into a single minimum. The solid lines in **a** are predictions based on independently measured single electron partitioning probabilities (Supplementary Fig. S5). **d-f**, Multivariate cumulants $\kappa_1 \dots \kappa_N$ calculated from the measured probabilities shown in **a-c**. Solid lines in **e**, **f** are fits using the Ising model (1); in **d** two non-equivalent cumulants contribute to κ_2 (see Methods and Supplementary Note 5). The inset in **d** shows the evolution of κ_1 across the entire range, and the solid line is the partitioning probability $P_{(0,1)}$ of a single electron.

follows a binomial distribution, with electrons scattering at the Y-junction independently of each other. To induce correlations, we now group the electrons in 2 pairs, placed in adjacent SAW minima (Fig. 2b). An increase of the probability $P_{(2,2)}$ can be observed compared to the non-interacting case, indicating antibunching of the two electrons contained in each pair. Finally, many-body correlations, we place all 4 electrons in the same SAW minimum (Fig. 2c) and note a similar increase in $P_{(2,2)}$ but the maxima of $P_{(1,3)}$ and $P_{(3,1)}$ now exceed $P_{(2,2)}$. While the probabilities in 2b and 2c are qualitatively different, the multi-electron interdependencies in the droplet are difficult to interpret directly from the counting statistics.

MULTIVARIATE CUMULANTS

To better understand the nature of the many-electron state in the droplet, we aim to characterise its internal correlations and decompose them into irreducible components, known as cumulants. Cumulants are convenient as they capture not only pairwise but also higher-order correlations. This is crucial for understanding complex many-body systems where

strong enough pairwise interactions can lead to correlations of all orders, heralding the emergence of a new collective state. One can consider the high-order cumulants $\langle\langle n^k \rangle\rangle$, or their combinations such as skewness and kurtosis, of the collective variable n , as it is measured directly [2, 28]. Yet, in this representation, contributions of individual particles are not resolved. To elucidate few-electron correlation effects, it is crucial to separate these correlations by order, corresponding to the number of electrons involved. We achieve this by recognizing that $n = T_1 + T_2 + \dots + T_N$ is a sum of multiple variables T_j , each corresponding to the partitioning outcome of the j^{th} electron ($T_j = 1$ if detected at D1 and 0 at D2). We consider the irreducible correlation functions $\langle\langle T_i T_j \dots T_k \rangle\rangle$, known as multivariate cumulants in statistics [35] or connected diagrams in field theory, to quantify the effect of interactions. Importantly, if the i^{th} electron is not interacting with the j^{th} electron, all multivariate cumulants involving both T_i and T_j will be zero.

Here we focus on the symmetrised multivariate cumulants κ_k defined by averaging the cumulants over all possible combinations of exactly k distinct variables T_j out of N . If electrons are statistically indistinguishable (all placed in the same SAW minimum, or all in different SAW minima), all terms in the averaging are equal and $\kappa_k = \langle\langle T_1 T_2 \dots T_k \rangle\rangle$. In this case, the multivariate cumulants κ_k are entirely determined by the counting probability distribution $P_{(N-n, n)}$, and can be computed from both measurements and models (see Methods).

We now use our experimental data to calculate the multivariate cumulants $(\kappa_1, \dots, \kappa_4)$ for the partitioning of 4 electrons as shown in panels d-f in Fig. 2. Let us start discussing panel 2d. In this case, the 4 electrons are loaded into different SAW minima, and as expected, for a binomial distribution, all higher-order cumulants $\kappa_{k>1}$ are zero. Since the first order cumulant κ_1 can be interpreted as the average number of transmitted electrons $\kappa_1 = \langle T_1 \rangle = \langle n \rangle / N$ detected in D1, the inset illustrates the random scattering of a single electron. The second central moment $\langle\langle n^2 \rangle\rangle = \langle n^2 \rangle - \langle n \rangle^2$ can be expressed in terms of the first two multivariate cumulants as $N\kappa_1(1 - \kappa_1) + N(N - 1)\kappa_2$. In the case of non-interacting electrons where $\kappa_2 = 0$, the second term vanishes, leaving only the first term which corresponds to pure shot noise accumulation.

Influence of interactions on cumulants becomes apparent in panel 2e where the scenario with two electrons in each of two adjacent SAW minima is examined. Here κ_2 is negative due to Coulomb repulsion between electrons in the same minimum. However, κ_3 and κ_4 are zero, indicating no interactions between electrons in different SAW minima (see Supplementary Note 5 for details). Higher-order correlations are revealed when all four electrons are placed in the same minimum (panel 2f). We observe that all cumulants κ_k up to the 4-th order are generally nonzero. Higher-order cumulants oscillate and exhibit $k - 1$ extrema separated by $k - 2$ zeros. Even cumulants are symmetrical, while odd cumulants are antisymmetrical, reflecting the symmetry of the Y-junction already evident from the partitioning probabilities in panels 2a-c.

EFFECTIVE ISING MODEL

Building on insights from high-energy colliders, we map the observed correlations onto the phase diagram of strongly correlated matter appropriate to our particular domain. In QCD at low baryonic densities [36], the transition from quark-gluon plasma at $T > T_c$ to hadronic fluid at $T < T_c$ is not a sharp phase transition but rather a crossover [37, 38] with $k_B T_c \sim 170$ MeV. Freeze-out of fluctuations (due to quench of equilibrium during expansion [14]) determines the cumulants in the number of produced hadrons, which can be used to connect QCD calculations to the statistics from collision experiments [2]. In analogy, the relevant

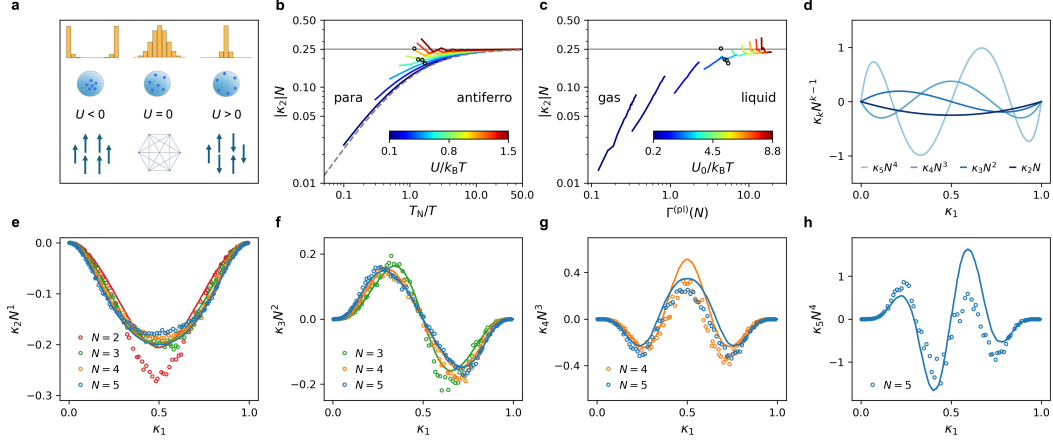


Fig. 3. **Scaling of correlation functions with the number of particles.** **a**, Interpretation of partitioning in terms of magnetic spin interactions. Uncorrelated partitioning ($U = 0$, binomial distribution in the middle), bunching ($U < 0$) and anti-bunching ($U > 0$) correspond, respectively, to paramagnetic, ferromagnetic and antiferromagnetic phases of an Ising model on a complete graph, for which counting statistics gives the distribution of total magnetization. **b**, Scaling of the second-order cumulant $|\kappa_2|$ with the number of particles $N = 2$ to 80 at the symmetric point ($\kappa_1 = 0.5$) and for different strengths of antiferromagnetic interaction $U/k_B T$ plotted against inverse temperature scaled by the Néel temperature T_N of the Ising model. The dashed line is the thermodynamic limit $N \rightarrow \infty$. Symbols mark experimental values for $N = 2 \dots 5$ with $U/k_B T$ of the Ising model fitted to match corresponding counting statistics (Extended Data Table 1). **c**, Scaled cumulant $|\kappa_2|N$ for the Coulomb liquid Monte Carlo simulations, as function of the plasma parameter $\Gamma^{(pl)}$ for $N = 2$ to 20. **d**, Universal pattern of correlations in the antiferromagnetic phase given by ultraspherical polynomials for $k = 2 \dots 5$. **e-h**, Measured cumulants κ_k of order $k = 2 \dots 5$ for droplets with $N = k \dots 5$. Data are compared to Monte Carlo simulations of a Coulomb liquid made of N electrons with interaction parameter $U_0 = 3.0 k_B T$.

state of matter for our electrons droplets is a one-component Coulomb plasma [39] with a crossover from a Coulomb gas at $T > T_N$ to a Coulomb liquid at $T < T_N$. The crossover temperature T_N is determined by the dimensionless plasma parameter $\Gamma^{(pl)} \sim T_N/T$. Unlike in QCD, where particle creation occurs, the corresponding equilibrium ensemble here is canonical, as no additional particles are generated. In the spirit of paradigmatic lattice-gas models [40], we derive the phase diagram and the finite-size scaling of our electron liquid droplets from the Ising model on a complete graph (all-to-all interactions), defined by the following Hamiltonian in terms of directly measurable partitioning variables,

$$\mathcal{H} = U \sum_{\substack{i,j=1 \\ i \neq j}}^N \left(T_i - \frac{1}{2}\right) \left(T_j - \frac{1}{2}\right) + \mu \sum_{i=1}^N T_i. \quad (1)$$

Here U is the interaction strength and μ controls the overall charge balance between two detectors with $\mu = 0$ corresponding to symmetric partitioning statistics, $P_{(n,m)} = P_{(m,n)}$.

The Ising model establishes a useful analogy between the phases of magnetically interacting effective spins $s_i = 2T_i - 1 = \pm 1$ and the partitioning statistics, see Fig. 3a. Coulomb antibunching implies $U > 0$ and the gas-to-liquid transition corresponds to the paramagnetic

to antiferromagnetic crossover of Ising spins with Néel temperature $k_B T_N = 2\kappa_1(1 - \kappa_1)UN$ in large- N (thermodynamic) limit (see Methods). Multivariate cumulants κ_k serve as Ising spin correlation functions and can therefore be used as order parameters to quantitatively trace this crossover, as illustrated in Fig. 3b and c. The signatures of a gas phase (Ising paramagnet, $T \gg T_N$) are small, N -independent cumulants (perturbative $\kappa_k \propto U^{k-1}$) while at low temperatures ($T \ll T_N$), universal antiferromagnetic correlations characteristic of an incompressible liquid set in with $\kappa_k N^{k-1}$ converging to well-defined polynomials in κ_1 , see Fig. 3d. We augment the coarse-grained effective Ising model with an explicit microscopic model of a 2D Coulomb plasma confined in a parabolic potential [41] (see Methods). Monte Carlo simulations of such finite Coulomb droplets show similar evolution of the order parameter if use the classical plasma parameter [30] $\Gamma^{(pl)}$ as a proxy for T_N/T , cf. Fig. 3b and c.

EVIDENCE FOR COULOMB LIQUID REGIME

The collider experiment gives access to κ_k as function of N and the detuning voltage Δ . We give three lines of evidence indicating that the electron droplets are already in the Coulomb liquid regime for $N \geq 3$. First, we find that the Ising model (1) describes accurately the measured cumulants as function of $\mu = -\alpha(\Delta - \Delta_0)$ (Fig. 2e,f and Extended Data Fig. 1 and 2) with $U/k_B T$ and Δ_0 fitted for each N independently and voltage-to-energy conversion α factor fixed globally (values listed in Extended Data Table 1). Placing the corresponding points in Fig. 3b shows that $T < T_N$ and the order parameter $|\kappa_2 N|$ is close to saturation. Secondly, we plot the experimentally measured quantities $\kappa_k N^{k-1}$ as a function of κ_1 in Fig. 3e-h. We observe that the predicted oscillation pattern and the scaling with N is obeyed. The amplitude of the oscillations is in good agreement with the universal limit shown in Fig. 3d, even for the modest values of N accessible in the experiment. Deviations mainly arise for κ_1 close to 0 or 1 where the Néel temperature goes to zero. Finally, we compare the measured fingerprints of strong partitioning correlations to the Coulomb droplet model with a single relevant parameter $U_0/k_B T = 3.0$ (U_0 is the characteristic energy scale for Coulomb interaction and the external parabolic potential [17, 41]) adjusted to match the observations, see lines in Fig. 3e-h and the dots in Fig. 3c. Despite considerable simplifications, we find very good agreement and conclude that our many-electron state behaves as a Coulomb liquid at plasma parameter $\Gamma^{(pl)} \approx 5$. An estimate of the effective temperature of the electron droplet $T = 30$ K (Supplementary Note 2) aligns with the assumption of a classical plasma and yields a Coulomb interaction energy of $U \approx 2$ to 3 meV, which is typical for confined electrons in GaAs.

CONCLUSION AND OUTLOOK

Inspired by the methodologies used to investigate quark-gluon plasma in relativistic ion colliders, we have realised a multi-electron collider on a microelectronic chip. Our highly-controlled partitioning experiments of electron droplets, containing up to five electrons, are analysed using multivariate cumulants. Remarkably, the observed correlated behaviour aligns well with an Ising model on a complete graph. The electron antibunching, driven by Coulomb interactions, can be effectively interpreted as antiferromagnetic ordering below Néel temperature. More broadly, our system can be analysed within the framework of liquid-gas transitions, where the electron droplet is best understood as a Coulomb liquid phase, similar to the incompressible liquid of hadrons bound by the nuclear force. Unlike high-energy ion collisions, we were able to trace universal signatures of collectivity at low multiplicities (particle number).

In the future, it would be highly interesting to extend this methodology to lower effective temperatures and strong magnetic fields, where quantum Hall states emerge in two-dimensional electron systems [30] and have been simulated for small number of particles [42]. Evidence of electron bunching has already been observed in pair partitioning experiments under high magnetic field [43], potentially indicating the formation of a Laughlin state droplet [44].

ACKNOWLEDGEMENTS

The authors acknowledge fruitful discussions with Urs Achim Wiedemann and Davis Zavriskis during the preparation of this manuscript. This project has received funding from the European Union H2020 research and innovation program under grant agreement No. 862683, “UltraFastNano”. C.B., H.S., and J.S. acknowledge funding from the Agence Nationale de la Recherche under the France 2030 programme, reference ANR-22-PETQ-0012. C.B. acknowledges financial support from the French Agence Nationale de la Recherche (ANR) project QUABS ANR-21-CE47-0013-01. J.W. acknowledges the European Union H2020 research and innovation program under the Marie Skłodowska-Curie grant agreement No. 754303. M.A. acknowledges the MSCA co-fund QuanG Grant No. 101081458, funded by the European Union. T.V. acknowledges funding from the French Laboratory of Excellence project “LANEF” (ANR-10-LABX-0051). A.D.W. and A.L. thank the DFG via ML4Q EXC 2004/1 - 390534769, the BMBF-QR.X Project 16KISQ009 and the DFH/UFA Project CDFA-05-06. E.P., R.S. and V.K. have been supported by Latvian Quantum Initiative within European Union Recovery and Resilience Facility project no. 2.3.1.1.i.0/1/22/I/CFLA/001 and grant no. lzp2021/1-0232 from the Latvian Council of Science.

Views and opinions expressed are those of the authors only and do not necessarily reflect those of the European Union or the granting authority. Neither the European Union nor the granting authority can be held responsible for them.

AUTHOR CONTRIBUTIONS

J.S. performed the experiment with expert help from J.W. and technical support from T.V., M.A., L.M, C.G and M.U. J.W. fabricated the sample. E.P. performed the cumulant calculations and R.S. the Monte Carlo simulations with guidance from V.K. A.L and A.D.W. provided the high-quality GaAs/GaAlAs heterostructure. J.S, E.P, C.B, V.K. and H.S. wrote the manuscript with feedback from all authors. H.S and C.B. supervised the experimental work. V.K. conceptualized the theoretical interpretation. C.B. has initiated the project.

METHODS

Device description

The device is fabricated in a Si-doped GaAs/AlGaAs heterostructure grown by molecular beam epitaxy (MBE). The two-dimensional electron gas (2DEG) resides 110 nm below the surface, with electron density $n \approx 2.8 \times 10^{11} \text{ cm}^{-2}$ and mobility $\mu \approx 9 \times 10^5 \text{ cm}^2/\text{V/s}$. Metallic gates (Ti, 3 nm; Au, 14 nm) are deposited on the surface of the semiconductor using electron-beam lithography. All measurements are performed at a temperature of about 20 mK in a $^3\text{He}/^4\text{He}$ dilution refrigerator. The sample and measurement scheme are the same as in Ref. [16]. A set of negative gate voltages is applied to the surface gates to deplete the 2DEG underneath and create the nanostructures, including 4 quantum dots (QD), 4 quantum point contacts (QPC), and 2 guiding rails which are fully depleted. These rails connect the source QDs to the detector QDs and merge in the centre to form a single 40- μm -long channel, equipped with a narrow barrier gate in the middle to tune the shape of the confining potential from a single well to a double well.

SAW generation

The surface acoustic wave (SAW) is generated using a regular interdigital transducer (IDT) deposited on the surface and placed at a distance of 3 mm from the device. The metallic fingers are fabricated using electron-beam lithography and thin-film evaporation (Ti, 3 nm; Al, 27 nm) on the heterostructure. The IDT consists of 111 cells with a periodicity of 1 μm and a resonance frequency $f_r \approx 2.86 \text{ GHz}$ at low temperature. The aperture of the transducer is 50 μm . To perform electron transport by SAW, a radiofrequency signal is applied on the IDT at its resonance frequency for a duration of 60 ns. To have a strong SAW confinement potential, the signal is amplified to 28 dB using a high-power amplifier (ZHL-4W-422+) before being injected into a coaxial line of the cryostat. The velocity of the SAW is 2860 m s^{-1} .

Electron transfer

Each single-shot experiment correspond to the transfer of one or a few electrons from the source QDs to the detector QDs using the SAW as transport carrier. To load electrons in the source QDs, we employ a sequence of fast voltage changes to the channel gate and reservoir gate controlling the tunnel barriers of the QD. This sequence consists of three steps: initializing the QD, loading the electrons into the QD, and preparing the QD for electron transfer. To initialise the source QD, electrons previously present in the QDs are removed. Then, a given number of electrons is loaded into the QD by accessing a particular loading position in the charge stability diagram of the QD. Finally, these electrons are trapped within the QD by switching to a holding configuration, from where they will be taken away by the SAW. A reference gate configuration is used to determine the electron number in the QD by comparing the QPC current before and after each step when tuning the system. Simultaneously, the detector QDs are set in a configuration for which the electrons transported by the SAW will be captured with high fidelity. By sensing the QPC currents of both the source and detector QDs before and after the electrons are transferred by the SAW, the precise number of electrons transferred to each detector can be determined. To calculate the detection probability, we use a post-selection method, where events that do not conserve the total number of electrons are excluded.

In our experiment, the electrons are not randomly transported by the SAW but are instead confined to specific locations within the SAW train. This precise control allows for

the formation of an electron droplet containing up to 5 electrons, using the two source QDs. The plunger gate is used to trigger the sending of the electrons into a precise minimum of the periodic SAW potential with a 30 ps resolution. To synchronise the trigger pulses of the two source QDs with the RF signal generating the SAW, we use two M8195A Keysight arbitrary waveform generators (AWG) combined with a synchronization module Keysight M8197A. The outputs of the AWGs are connected to the plunger gates via high-bandwidth bias tees (SHF BT45A) for dc-biasing.

Electron partitioning

The electron droplet is partitioned at the Y-junction located at the end of the central channel, after a flight time of 14 ns. By applying a voltage detuning $\Delta = V_U - V_L$, where V_U and V_L are the voltages applied to the side gates of the central channel, we can control the partitioning ratio between the two detectors. For all partitioning experiments reported here, the barrier gate voltage is set to $V_B = -1.25$ V to have a single central channel with a weak double-well potential profile (there is full charge transfer between the upper and lower rails during the electron transport along the central channel).

Symmetrised multivariate cumulants

From $n = T_1 + \dots + T_N$ and $T_j^2 = T_j$, we derive the general relation

$$m_k = \binom{N}{k}^{-1} \sum_{n=k}^N \binom{n}{k} p_n \quad (2)$$

between the probabilities p_n of the FCS and the k -th order symmetrised multivariate moments m_k defined as averages of all permutations of k distinct variables,

$$m_k = \binom{N}{k}^{-1} \sum_{1 \leq j_1 < j_2 < \dots < j_N \leq N} \langle T_{j_1} T_{j_2} \dots T_{j_k} \rangle \quad (3)$$

where $\binom{N}{k} = N!/[k!(N-k)!]$ is the binomial coefficient.

The corresponding symmetrised multivariate cumulants,

$$\kappa_k = \binom{N}{k}^{-1} \sum_{1 \leq j_1 < j_2 < \dots < j_N \leq N} \langle\langle T_{j_1} T_{j_2} \dots T_{j_k} \rangle\rangle, \quad (4)$$

in general, are not uniquely determined for FCS and their calculation requires additional information (such as symmetry constraints or a microscopic model). Rescaling to spin variables, $s_i = 2T_i - 1$, transforms the cumulants as $\langle\langle s_j \rangle\rangle = 2\kappa_1 - 1$ and $\langle\langle s_1 \dots s_k \rangle\rangle = 2^k \kappa_k$ for $k \geq 2$.

For statistically equivalent particles (i.e., full permutational symmetry of the multivariate probability distribution), all terms in Eq. (3) and in Eq. (4) are equal, and the moments m_k can be related to cumulants κ_k via standard univariate relations [45], $\ln(1 + \sum_{k=1}^{\infty} m_k z^k/k!) = \sum_{k=1}^{\infty} \kappa_k z^k/k!$. Using an explicit formula in terms of Bell polynomials [46] and Eq. (2), we can write

$$\kappa_k = \sum_{j=1}^k (j-1)! (-1)^{j-1} B_{kj} \left(\frac{\langle n \rangle}{N}, \frac{\langle (n)_2 \rangle}{(N)_2}, \dots, \frac{\langle (n)_{k-j+1} \rangle}{(N)_{k-j+1}} \right). \quad (5)$$

where $(x)_k = x(x-1) \times \dots \times (x-k+1)$ is the falling factorial, and B_{kj} is the incomplete Bell polynomial. See Supplementary note 4 for derivation of Eq. (2) and explicit formulas for κ_k for $k = 1$ to 5. An example of correlated partitioning where (5) is not valid and the general combinatorial expressions for multivariate cumulants [35, 47] need to be used is illustrated in Fig. 2e and described in detail in Supplementary note 5.

Note that $\langle\langle n \rangle\rangle_k$ is known as the factorial moment of the FCS. The corresponding factorial cumulants $\langle\langle n^k \rangle\rangle_F$ have been considered as signatures of interactions in the context of electron transport [29] and particle physics [48]. We observe that $\langle\langle n^k \rangle\rangle_F \neq \kappa_k$ because of the additional factor $(N)_k$ in the relation between the multivariate moment m_k and the FCS factorial moment, $m_k = \langle\langle n \rangle\rangle_k / (N)_k$.

Ising model on a complete graph

Ising model on a complete graph is exactly solvable [49] and hence equilibrium fluctuations of at any freeze-out temperature T can be computed for any N . The Hamiltonian (1) can be expressed in terms of $n = \sum_{j=1}^N T_j$ as $\mathcal{H} = Un^2 + (\mu - NU)n + N(N-1)U/4$. The corresponding exact counting statistics in a canonical ensemble is $p_n = c_n/Z$ with the partition function $Z = \sum_{n=0}^N c_n$ and the statistical weights

$$c_n = \binom{N}{n} e^{-\beta Un(N-n) - \mu n}. \quad (6)$$

where $\beta = 1/k_B T$. Together with Eq. (5), this gives exact multivariate cumulants of all orders $k \leq N$.

To derive the relations for the cumulants κ_k in the thermodynamic limit, we apply lowest-order Stirling's formula to the binomial coefficient, and obtain a Gaussian approximation to p_n of the form

$$p_n \propto \exp[-(\beta + \beta_N)U(n - \kappa_1 N)^2], \quad (7)$$

where $\beta_N = 1/k_B T_N$ is the inverse of the Néel temperature (for $U > 0$) given by

$$k_B T_N = 2\kappa_1(1 - \kappa_1)UN. \quad (8)$$

From $N_c/N = T/T_N$, we identify the characteristic droplet size N_c at which the crossover takes place

$$N_c = [2\kappa_1(1 - \kappa_1)\beta U]^{-1}. \quad (9)$$

We then compute the second central moment $\langle\langle n^2 \rangle\rangle = \langle n^2 \rangle - \langle n \rangle^2$ (also called second-order univariate cumulant) using Eq. (7) and extract the second-order multivariate cumulant κ_2 from the identity $\langle\langle n^2 \rangle\rangle = N\kappa_1(1 - \kappa_1) + N(N-1)\kappa_2$ in the large N limit. The resulting expression

$$N\kappa_2 = -\frac{\kappa_1(1 - \kappa_1)}{1 + N_c/N}. \quad (10)$$

describes the scaling of this cumulant across the crossover from paramagnetic ($N \ll N_c$) to antiferromagnetic ($N \gg N_c$) state of the Ising model. This asymptotic relation is drawn with a dashed line in Fig. 3(b) for $\kappa_1 = 0.5$.

As there is no lattice favoring a particular pattern of staggered magnetization, the antiferromagnetic transition is not a second-order phase transition but a crossover. The corresponding change in free energy has a weaker divergence ($\log N$) in the thermodynamic limit than at the ferromagnetic transition. The corresponding singular part [40] of the free energy change in the range between $T = \infty$ and $T \rightarrow 0^+$ is $\beta\Delta F_{U>0} = (1/2)\ln(1 + T_N/T)$. On the ferromagnetic side ($U < 0$), we note that $\kappa_2 N$ diverges at the Curie temperature $T_C = -T_N > 0$ as $\kappa_2 N \propto (T - T_C)^{-1}$ for $T \rightarrow T_C^+$. At $T \leq T_C$, the Gaussian approximation (7) breaks down and strong ferromagnetic order sets in with $\kappa_2 = \kappa_1(1 - \kappa_1) > 0$ in the thermodynamic limit. The corresponding free energy change between $T = \infty$ and $T \rightarrow T_C^+$ is $\beta\Delta F_{U<0} = (1/2)\ln(1 - T_C/T)$.

Universal scaling of partitioning cumulants

Interaction-dominated partitioning of a large droplet at $U > 0$ is described by the antiferromagnetic phase of the effective Ising model with $T/T_N \rightarrow 0$ and $N \rightarrow \infty$. The Boltzmann factor in Eq. (6) leads to exponential suppression of fluctuations of n around $\langle n \rangle = \kappa_1 N$ and caps the large- N asymptotics of univariate cumulants from $\langle\langle n^k \rangle\rangle = O(N)$ (Gaussian limit of binomial distribution) to $\langle\langle n^k \rangle\rangle = O(1)$. This leads to the asymptotics $\kappa_k = G_k(\kappa_1)N^{-k+1} + O(N^{-k})$ for $k \geq 2$ where the prefactor

$$G_k(\kappa_1) = -\frac{(k-1)!}{2} C_k^{(-1/2)}(2\kappa_1 - 1) \quad (11)$$

is universal and given by the ultraspherical (Gegenbauer) polynomials $C_k^{(a)}$ of degree k and parameter $a = -1/2$. First polynomials up to $k = 5$ are shown in Fig. 3d, $G_2 = -\kappa_1(1 - \kappa_1)$ is also the limit of Eq.(10).

The polynomials $G_k(\kappa_1)$ have exactly $k - 2$ zeros for $0 < \kappa_1 < 1$ which explains the observed oscillation pattern, and provides an exact specific example of oscillations in high-order cumulants [28]. We note that a similar generic N^{-k+1} scaling has been discussed for cumulants of initial density perturbations in heavy ion collisions [50] where it arises for different reasons (dominance of autocorrelations in independent point sources model).

In contrast to antiferromagnetic correlations decaying with N as $\kappa_k \propto N^{-k+1}$, the ferromagnetic order for $U < 0$ is rigid with $\kappa_k = O(1)$ and the limiting form for $T/T_C \rightarrow 0$ also being a polynomial, $\kappa_k = -\text{Li}_{1-k}(\frac{\kappa_1}{\kappa_1-1})$, where Li is the polylogarithm.

Coulomb droplet model

We model a finite droplet of Coulomb plasma in 2D using a symmetric parabolic confinement and an unscreened Coulomb potential [41] described by the interaction potential

$$U(\mathbf{r}_1, \dots, \mathbf{r}_N) = \frac{m\omega_0^2}{2} \sum_{i=1}^N \mathbf{r}_i^2 + \sum_{i<j} \frac{e^2}{4\pi\epsilon_0\epsilon_r|\mathbf{r}_i - \mathbf{r}_j|}, \quad (12)$$

where $\mathbf{r}_j = (x_j, y_j)$ is the in-plane coordinate of j -th electron, ω_0 controls the strength of the electrostatic confinement, $\epsilon_0\epsilon_r$ and m are the electric permittivity and effective electron mass in GaAs, respectively.

The equilibrium distribution of electron coordinates is determined by a canonical ensemble with inverse temperature $k_B\beta$. Using the characteristic length $d_0 = [2e^2/(4\pi\epsilon_0\epsilon_r m\omega_0^2)]^{1/3}$ and energy $U_0 = e^2/(4\pi\epsilon_0\epsilon_r d_0)$ [17, 41], the distribution of the dimensionless coordinate $\tilde{y}_j = y_j/d_0$ in the y direction (transverse to the Y-junction) is completely determined by the dimensionless interaction parameter βU_0 and by the number N of electrons. We sample

\tilde{y}_j using Metropolis Monte Carlo algorithm, controlling convergence of the corresponding Markov chain with Geweke's diagnostic [51]. A set of 10^5 samples is produced for each βU_0 and each N .

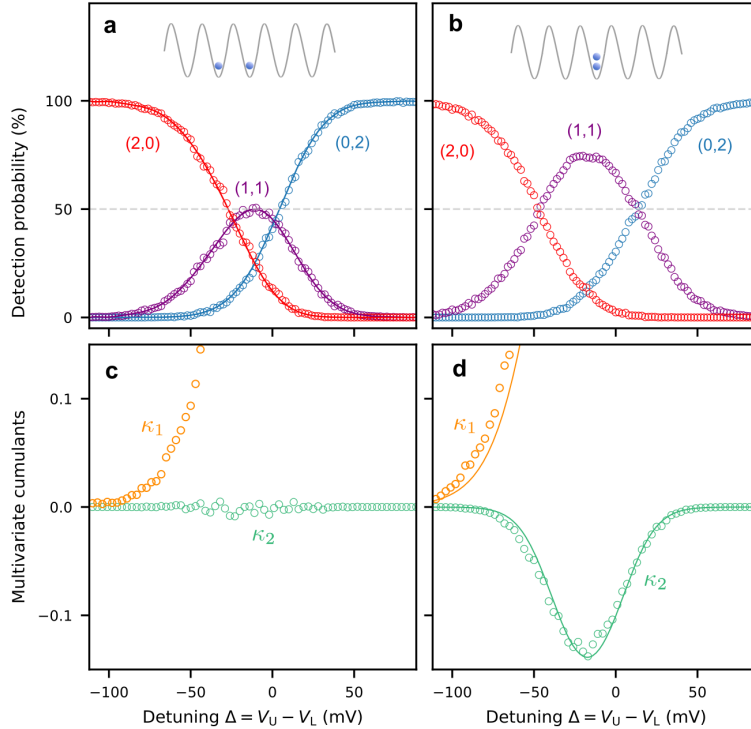
Partitioning statistics of a sudden quench is computed with counting variables of the form $T_j = \Theta(y_j - b)$ where Θ is the step function. This simple form allows calculations of T_j as functions of the impact parameter b from each Monte Carlo sample and thus greatly speeds up the calculation of the multivariate cumulants as function of κ_1 that is presented in Fig. 3.

In our experiment, the symmetry plane of the Y-junction is fixed and the impact parameter b can be tuned by the voltage difference Δ on the side gates, with the correspondence $b = e\mathcal{E}_y d_0/(2U_0)$ where $\mathcal{E}_y \propto \Delta - \Delta_0$ is the transverse electric field. The symmetry point Δ_0 of the partitioning corresponds to the origin of the y coordinates in the Coulomb droplet model of Eq. (12).

In the thermodynamic limit of large N , our model corresponds to a one-component plasma [39]. To calculate the plasma parameter $\Gamma^{(pl)} = \beta U_0 \sqrt{\pi n_e}$, the dimensionless number density n_e is estimated as d_0^2/a^2 , where a is the average distance to the nearest electron, over all N electrons in all 10^5 Monte Carlo samples.

The plasma parameter of each experimental point reported as a symbol in Fig. 3(c) is taken equal to that of the Monte Carlo simulation with the same N and $\beta U_0 = 3$, since these simulations are matching the overall pattern of experimental data in Fig. 3(e-h).

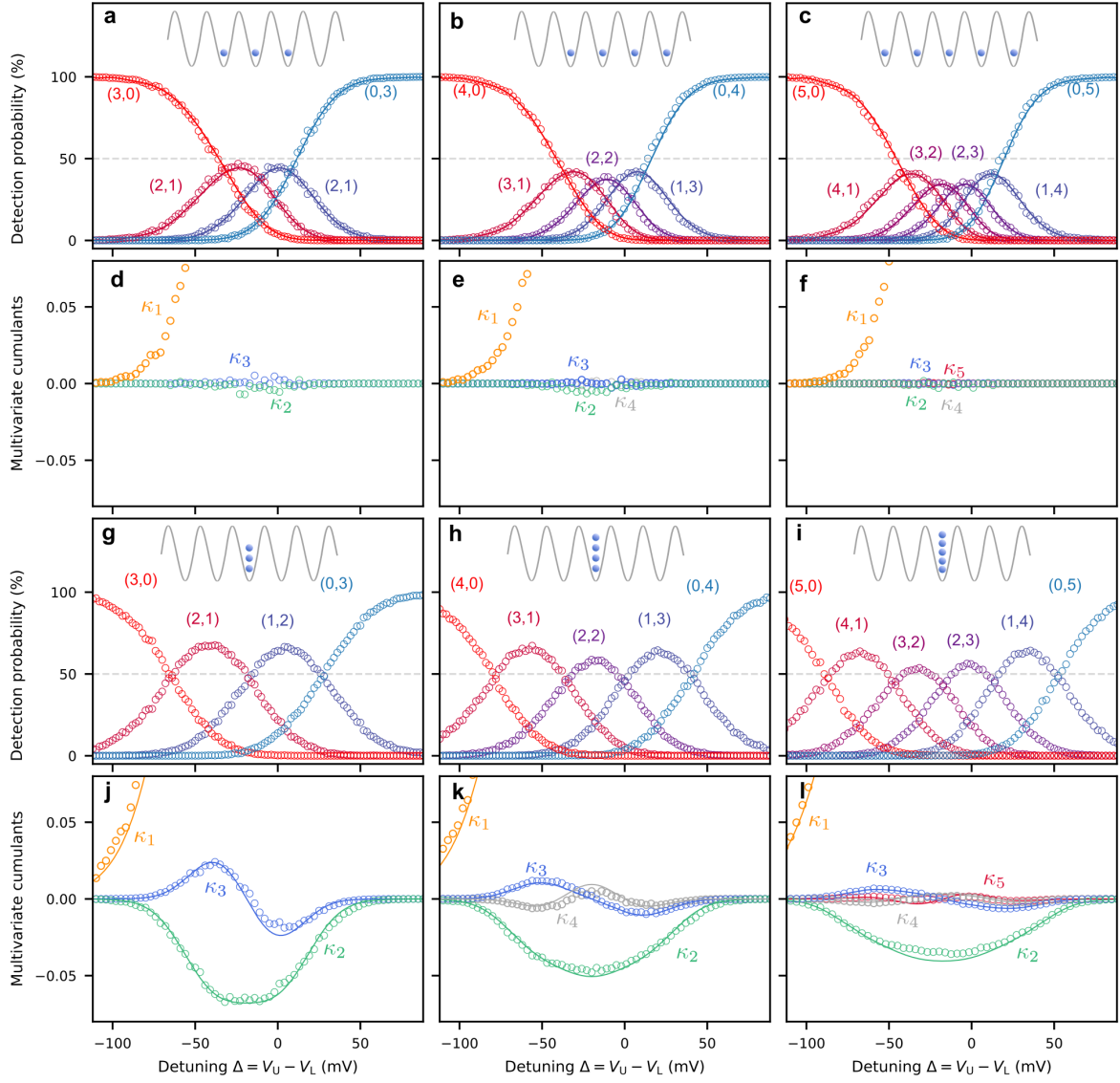
EXTENDED DATA FIGURES AND TABLES



Extended Data Fig. 1. **Experimental data for partitioning of $N = 2$ electrons.** **a**, Partitioning probabilities when the two electrons are distributed in two different minima and are uncorrelated. **b**, Partitioning probabilities when both electrons are in the same SAW minimum and are interacting. Panels **c** and **d** display the multivariate cumulants corresponding to **a** and **b**, respectively. Solid lines in **a** are reconstructions using single-electron partitioning data, and lines in **d** are fitting curves from the Ising model using the parameters given in Extended Data Table 1.

N	Δ_0 (mV)	$\alpha/k_B T$ (mV $^{-1}$)	$U/k_B T$	$U_{MC}/k_B T$
1	-10.8	0.062	–	–
2	-14.9	0.062	1.16	0.92
3	-18.3	0.062	0.89	0.85
4	-18.8	0.062	0.77	0.81
5	-17.7	0.062	0.67	0.77

Extended Data Table 1. **Model parameters.** Fitting parameters of the Ising model for partitioning experiments and Monte Carlo simulations of N electron droplets. The parameters Δ_0 , $\alpha/k_B T$ and $U/k_B T$ correspond to the partitioning experiments, while the parameter $U_{MC}/k_B T$ corresponds to the Monte Carlo simulations of Coulomb droplets with interaction parameter $U_0/k_B T = 3$.



Extended Data Fig. 2. **Experimental data for partitioning of $N = 3, 4, 5$ electrons.** Panels **a** to **f** show the partitioning probabilities and the corresponding multivariate cumulants for electrons distributed across different SAW minima (uncorrelated electrons). Panels **g** to **l** show the same quantities when all electrons are placed in the same SAW minimum (interacting electrons). Solid lines in **a-c** are reconstructions using single-electron partitioning data, and lines in **j-l** are fitting curves from the Ising model using the parameters given in Extended Data Table 1.

REFERENCES

- [1] P. W. Anderson, More is different: Broken symmetry and the nature of the hierarchical structure of science., *Science* **177**, 393 (1972).
- [2] S. Gupta, X. Luo, B. Mohanty, H. G. Ritter, and N. Xu, Scale for the phase diagram of quantum chromodynamics, *Science* **332**, 1525 (2011).
- [3] B. DeMarco and D. S. Jin, Onset of Fermi degeneracy in a trapped atomic gas, *Science* **285**, 1703 (1999).
- [4] I. Bloch, J. Dalibard, and S. Nascimbene, Quantum simulations with ultracold quantum gases, *Nature Physics* **8**, 267 (2012).
- [5] L. Saminadayar, D. C. Glatthli, Y. Jin, and B. Etienne, Observation of the $e/3$ fractionally charged Laughlin quasiparticle, *Physical Review Letters* **79**, 2526 (1997).
- [6] R. de Picciotto, M. Reznikov, M. Heiblum, M. Heiblum, V. Umansky, G. Bunin, and D. Mahalu, Direct observation of a fractional charge, *Nature* **389**, 162–164 (1997).
- [7] J. Dubois, T. Jullien, F. Portier, P. Roche, A. Cavanna, Y. Jin, W. Wegscheider, P. Roulleau, and D. C. Glatthli, Minimal-excitation states for electron quantum optics using levitons, *Nature* **502**, 659 (2013).
- [8] H. Bartolomei, M. Kumar, R. Bisognin, A. Marguerite, J. M. Berroir, E. Bocquillon, B. Plaças, A. Cavanna, Q. Dong, U. Gennser, and G. Fève, Fractional statistics in anyon collisions, *Science* **368**, 173 (2020).
- [9] J. F. Grosse-Oetringhaus and U. A. Wiedemann, A decade of collectivity in small systems, *arXiv preprint arXiv:2407.07484* (2024).
- [10] A. Wenz, G. Zürn, S. Murmann, I. Brouzos, T. Lompe, and S. Jochim, From few to many: observing the formation of a Fermi sea one atom at a time, *Science* **342**, 457 (2013).
- [11] J. W. Harris and B. Müller, The search for the quark-gluon plasma, *Annual Review of Nuclear and Particle Science* **46**, 71 (1996).
- [12] L. Adamczyk, J. K. Adkins, G. Agakishiev, M. M. Aggarwal, Z. Ahammed, I. Alekseev, J. Alford, C. D. Anson, A. Aparin, D. Arkhipkin, *et al.*, Energy dependence of moments of net-proton multiplicity distributions at RHIC, *Physical Review Letters* **112**, 032302 (2014).
- [13] K. Rajagopal and F. Wilczek, Static and dynamic critical phenomena at a second order QCD phase transition, *Nuclear Physics B* **399**, 395 (1993).
- [14] J. W. Harris and B. Müller, “QGP Signatures” revisited, *The European Physical Journal C* **84**, 247 (2024).
- [15] E. Bocquillon, V. Freulon, J. M. Berroir, P. Degiovanni, B. Plaças, A. Cavanna, Y. Jin, and G. Fève, Coherence and indistinguishability of single electrons emitted by independent sources, *Science* **339**, 1054 (2013).
- [16] J. Wang, H. Edlbauer, A. Richard, S. Ota, W. Park, J. Shim, A. Ludwig, A. D. Wieck, H. S. Sim, M. Urdampilleta, *et al.*, Coulomb-mediated antibunching of an electron pair surfing on sound, *Nature Nanotechnology* **18**, 721 (2023).
- [17] N. Ubbelohde, L. Freise, E. Pavlovska, P. G. Silvestrov, P. Recher, M. Kokainis, G. Barinova, F. Hohls, T. Weimann, K. Pierz, *et al.*, Two electrons interacting at a mesoscopic beam splitter, *Nature Nanotechnology* **18**, 733 (2023).
- [18] J. D. Fletcher, W. Park, S. Ryu, P. See, J. P. Griffiths, G. A. C. Jones, I. Farrer, D. A. Ritchie, H. S. Sim, and M. Kataoka, Time-resolved Coulomb collision of single electrons, *Nature Nanotechnology* **18**, 727 (2023).
- [19] W. Lu, Z. Ji, L. Pfeiffer, K. W. West, and A. J. Rimberg, Real-time detection of electron

- tunnelling in a quantum dot, *Nature* **423**, 422 (2003).
- [20] T. Fujisawa, T. Hayashi, R. Tomita, and Y. Hirayama, Bidirectional counting of single electrons, *Science* **312**, 1634 (2006).
- [21] S. Gustavsson, R. Leturcq, B. Simovič, R. Schleser, T. Ihn, P. Studerus, K. Ensslin, D. C. Driscoll, and A. C. Gossard, Counting statistics of single electron transport in a quantum dot, *Physical Review Letters* **96**, 076605 (2006).
- [22] N. Ubbelohde, C. Fricke, C. Flindt, F. Hohls, and R. J. Haug, Measurement of finite-frequency current statistics in a single-electron transistor, *Nature Communications* **3**, 612 (2012).
- [23] J. Bylander, T. Duty, and P. Delsing, Current measurement by real-time counting of single electrons, *Nature* **434**, 361 (2005).
- [24] Y. Bomze, G. Gershon, D. Shovkun, L. Levitov, and M. Reznikov, Measurement of counting statistics of electron transport in a tunnel junction, *Physical Review Letters* **95**, 176601 (2005).
- [25] B. Reulet, J. Senzier, and D. E. Prober, Environmental effects in the third moment of voltage fluctuations in a tunnel junction, *Physical Review Letters* **91**, 196601 (2003).
- [26] J. C. Forgues, F. B. Sane, S. Blanchard, L. Spietz, C. Lupien, and B. Reulet, Noise intensity-intensity correlations and the fourth cumulant of photo-assisted shot noise, *Scientific Reports* **3**, 2869 (2013).
- [27] G. Gershon, Y. Bomze, E. V. Sukhorukov, and M. Reznikov, Detection of non-gaussian fluctuations in a quantum point contact, *Physical Review Letters* **101**, 016803 (2008).
- [28] C. Flindt, C. Fricke, F. Hohls, T. Novotný, K. Netočný, T. Brandes, and R. J. Haug, Universal oscillations in counting statistics, *Proceedings of the National Academy of Sciences* **106**, 10116 (2009).
- [29] D. Kambly, C. Flindt, and M. Büttiker, Factorial cumulants reveal interactions in counting statistics, *Physical Review B* **83**, 075432 (2011).
- [30] Y. Monarkha and K. Kono, *Two-dimensional Coulomb liquids and solids*, Vol. 142 (Springer, 2013).
- [31] S. Hermelin, S. Takada, M. Yamamoto, S. Tarucha, A. D. Wieck, L. Saminadayar, C. Bäuerle, and T. Meunier, Electrons surfing on a sound wave as a platform for quantum optics with flying electrons, *Nature* **477**, 435 (2011).
- [32] R. McNeil, M. Kataoka, C. J. B. Ford, C. Barnes, D. Anderson, G. A. C. Jones, I. Farrer, and D. A. Ritchie, On-demand single-electron transfer between distant quantum dots, *Nature* **477**, 439 (2011).
- [33] S. Takada, H. Edlbauer, H. V. Lepage, J. Wang, P. A. Mortemousque, G. Georgiou, C. H. Barnes, C. J. Ford, M. Yuan, P. V. Santos, *et al.*, Sound-driven single-electron transfer in a circuit of coupled quantum rails, *Nature Communications* **10**, 4557 (2019).
- [34] H. Edlbauer, J. Wang, S. Ota, A. Richard, B. Jadot, P. A. Mortemousque, Y. Okazaki, S. Nakamura, T. Kadera, N. H. Kaneko, *et al.*, In-flight distribution of an electron within a surface acoustic wave, *Applied Physics Letters* **119**, 114004 (2021).
- [35] G. S. James and A. J. Mayne, Cumulants of functions of random variables, *Sankhyā: The Indian Journal of Statistics, Series A (1961-2002)* **24**, 47 (1962).
- [36] T. Niida and Y. Miake, Signatures of QGP at RHIC and the LHC, *AAPPS Bulletin* **31**, 12 (2021).
- [37] Y. Aoki, G. Endrődi, Z. Fodor, S. D. Katz, and K. K. Szabó, The order of the quantum chromodynamics transition predicted by the Standard Model of particle physics, *Nature* **443**, 675 (2006).
- [38] S. Borsanyi, G. Endrődi, Z. Fodor, A. Jakovac, S. D. Katz, S. Krieg, C. Ratti, and K. K.

- Szabó, The QCD equation of state with dynamical quarks, *Journal of High Energy Physics* **2010**, 77 (2010).
- [39] M. Baus and J. P. Hansen, Statistical mechanics of simple Coulomb systems, *Physics Reports* **59**, 1 (1980).
- [40] A. Pelissetto and E. Vicari, Critical phenomena and renormalization-group theory, *Physics Reports* **368**, 549 (2002).
- [41] V. M. Bedanov and F. M. Peeters, Ordering and phase transitions of charged particles in a classical finite two-dimensional system, *Physical Review B* **49**, 2667 (1994).
- [42] P. Lunt, P. Hill, J. Reiter, P. M. Preiss, M. Gałka, and S. Jochim, Realization of a Laughlin state of two rapidly rotating fermions, arXiv preprint arXiv:2402.14814 (2024).
- [43] N. Ubbelohde, F. Hohls, V. Kashcheyevs, T. Wagner, L. Fricke, B. Kästner, K. Pierz, H. W. Schumacher, and R. J. Haug, Partitioning of on-demand electron pairs, *Nature Nanotechnology* **10**, 46 (2015).
- [44] R. B. Laughlin, Quantized motion of three two-dimensional electrons in a strong magnetic field, *Physical Review B* **27**, 3383 (1983).
- [45] P. McCullagh, *Tensor methods in statistics: monographs on statistics and applied probability* (Chapman and Hall/CRC, 2018).
- [46] L. Comtet, *Advanced combinatorics* (Springer Dordrecht, 1974).
- [47] C. W. Gardiner, Handbook of stochastic methods - for physics, chemistry and the natural sciences, second edition, in *Springer Series in Synergetics* (1986).
- [48] M. Kitazawa and X. Luo, Properties and uses of factorial cumulants in relativistic heavy-ion collisions, *Physical Review C* **96**, 024910 (2017).
- [49] R. J. Baxter, *Exactly solved models in statistical mechanics* (Elsevier Science, 2016).
- [50] S. Floerchinger and U. A. Wiedemann, Statistics of initial density perturbations in heavy ion collisions and their fluid dynamic response, *Journal of High Energy Physics* **2014**, 5 (2014).
- [51] J. Geweke, Evaluating the accuracy of sampling-based approaches to the calculation of posterior moments (Oxford University Press, 1992).
- [52] U. Weiss and W. Haeffner, Complex-time path integrals beyond the stationary-phase approximation: decay of metastable states and quantum statistical metastability, *Physical Review D* **27**, 2916 (1983).
- [53] U. Weiss, *Quantum dissipative systems* (World Scientific, 2012).
- [54] P. Hänggi, P. Talkner, and M. Borkovec, Reaction-rate theory: fifty years after Kramers, *Reviews of Modern Physics* **62**, 251 (1990).
- [55] I. Affleck, Quantum-statistical metastability, *Physical Review Letters* **46**, 388 (1981).
- [56] L. S. Levitov, H. Lee, and G. B. Lesovik, Electron counting statistics and coherent states of electric current, *Journal of Mathematical Physics* **37**, 4845 (1996).

SUPPLEMENTARY MATERIAL

for

Partitioning statistics of a correlated few-electron droplet

CONTENTS

1. CONTROL OF MULTI-ELECTRON TRANSFER	20
1.1. Multi-electron loading technique	20
1.1.1. Placing all electrons in the same SAW minimum	20
1.1.2. Placing all electrons in different SAW minima	21
2. TUNING THE CENTRAL CHANNEL FOR $N = 1$ ELECTRON	25
2.1. Experimental data	25
2.2. Double-well model	25
2.2.1. Two-site master-equation model	25
2.2.2. Model for thermally activated hopping in a quartic double-well potential	27
3. RECONSTRUCTION FORMULA FOR N INDEPENDENT ELECTRONS	29
4. COUNTING STATISTICS AND CUMULANTS	30
4.1. Multivariate and univariate cumulants	30
4.2. Relation between symmetrised multivariate cumulants and univariate full counting statistics	31
4.3. Comparison of different types of cumulants for FCS	32
5. ANALYSIS OF $2e/2e$ ($N = 4$) PARTITIONING DATA	34

1. CONTROL OF MULTI-ELECTRON TRANSFER

To prepare a droplet of several electrons, precise control over electron placement in a selected potential minimum of the surface acoustic wave (SAW) is essential. This task is not straightforward and several parameters must be meticulously tuned and optimised. The procedure is described here.

1.1. Multi-electron loading technique

First, the two source quantum dots (QD) are initialised with the desired number of electrons, while the two detector QDs are left empty. The number of electrons in each QD is identified with the help of their respective loading map as shown in Fig. S1a. This map is obtained by measuring the current change through the quantum point contact (QPC) coupled to the QD. This charge sensing method provides a very accurate count of the QD electrons, as illustrated in Fig. S1b. Each pixel in the loading map represents the change in QPC current before and after a specific loading configuration controlled by the voltages V_R and V_C applied to the QD gates [33].

The system is then configured to a holding state, in which the electrons remains trapped in the QDs until the SAW arrives. The yellow regions of the holding maps in Fig. S1c,d represent the various sets of gate voltages for which the 3 electrons initially loaded in the source QD remains trapped.

These electrons are then transported by the SAW train in two distinct configurations: either in the same potential minimum, or in different potential minima.

1.1.1. *Placing all electrons in the same SAW minimum*

We discuss here the procedure for transporting all the electrons together in the same SAW minimum, thereby forming a single electron droplet. The sending process is configured independently for each source using a single detector. For this purpose, a large detuning Δ is applied to tilt the confinement potential of the central channel and direct all the electrons towards the selected detector.

Figure S2a,b show the holding and catching maps in absence of SAW, for the source and detector QDs, respectively (the axis correspond to the gate voltages of the *source* QD for both maps). No electron is transferred, as expected in absence of SAW. We then launch a 180 μm -long SAW train (60 ns of 3 GHz RF signal) and count the final number of electrons in the source and detector QDs to construct the sending and catching maps shown in Fig. S2c,d. For gate voltages in the bottom-right sector of the maps, 1, 2, or 3 electrons have been transferred as indicated by the specific amplitude of the QPC current change. However, the electrons transported in this way are not transferred in the same potential minimum of the SAW train, but in random minima. To load all the electrons into the same SAW minimum, the gate voltages are adjusted such that all the electrons remain in the source QD even as the SAW train passes by (top-right sector of the maps). Then, a very short negative RF pulse is applied to the plunger (P) gate of the source QD to rise the energy of the electrons and enable their catching and transport by the SAW, as shown in Fig. S2g,h. Applying an RF pulse with a time duration shorter than the SAW period ensures that the electrons are placed precisely into the designated SAW minimum. Both the amplitude (V_P) and the

time delay (δt_{trig}) of the trigger pulse are carefully calibrated to ensure that all electrons are loaded into the designated SAW minimum [16, 33]. The maps are used to select the optimal voltages V_C^{send} and V_R^{send} , applied to the channel gate (C) and reservoir gate (R) of the source QD. Once optimised, these values are used as the standard working point for the sending state in all subsequent experiments.

Since loading more than 3 electrons from a single source poses considerable technical challenges, sending 4 or 5 electrons is achieved by using the two sources S1 and S2 which are synchronised via their trigger pulse. For example, a droplet of $N = 5$ electrons is obtained by sending 3 electrons from S1 and 2 electrons from S2, all in the same SAW minimum. They are initially in different rails, but later join in the central channel.

For partitioning experiments with N electrons, the detector QDs must be tuned for catching up to N electrons. Fig. S3 shows the histograms of QPC current jumps from the two detectors (D1 and D2) for the partitioning data of $N = 5$ electrons in the same SAW minimum, demonstrating the detector capability of catching up to 5 electrons.

1.1.2. Placing all electrons in different SAW minima

To investigate the partitioning of uncorrelated electrons, we have to place the electrons in different SAW minima. This configuration is achieved by a combination of random and triggered electron sending, as well as a combination of the two electron sources S1 and S2. For the case of 3 electrons, we can proceed in the following ways.

A first possibility is to load 3 electrons in a single source and simply apply a SAW train without triggering the plunger gate. In this situation, the electrons are automatically distributed over 3 random SAW minima. This property is evidenced by the absence of correlation in the partitioning experiments performed in this way.

A second possibility is to load 2 electrons in the source S1 and one electron in the source S2. We can either use the random sending procedure of the 2 electrons of S1, while the electron in S2 is sent using a trigger pulse at a delayed time near the end of the SAW train, or send the first electron of S1 randomly and the second electron of S1 with a trigger pulse, while the electron of S2 is sent with a trigger pulse at a later time. All these procedures ensure that the 3 electrons are in 3 different SAW minima.

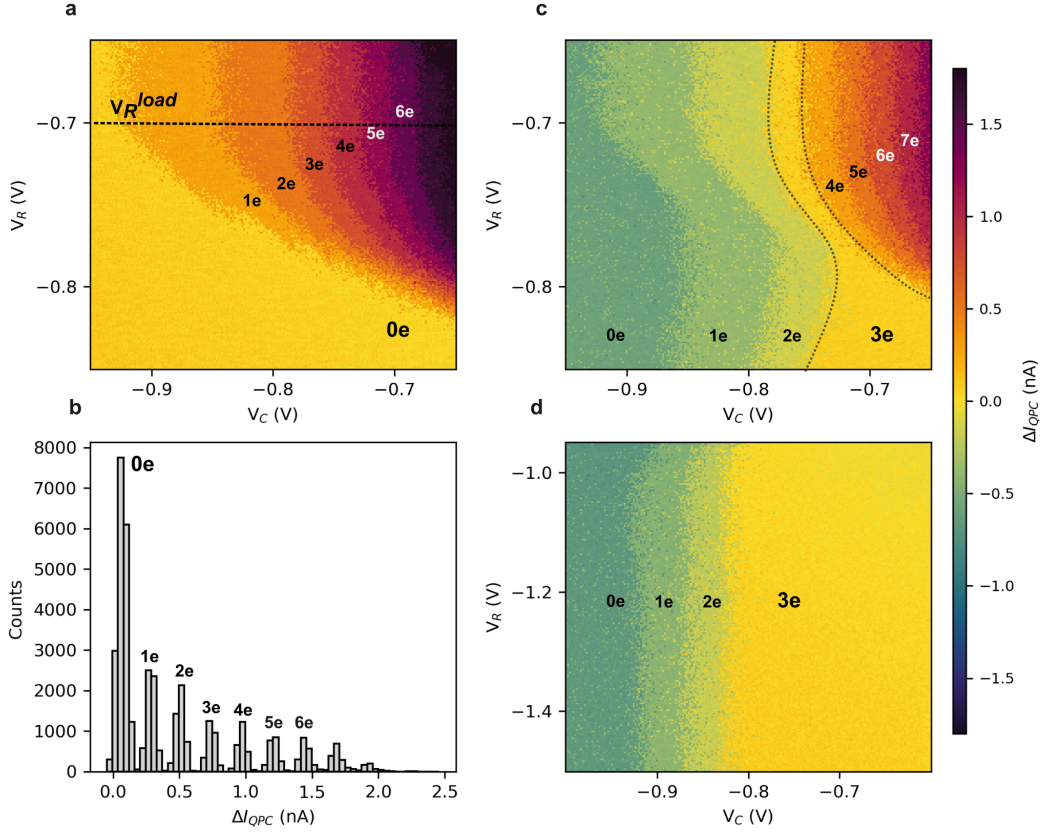


Fig. S1. **Loading and holding maps of a source quantum dot.** **a**, Loading map of the electron source S1. The axis V_R and V_C denote the reservoir (R) and channel (C) gate voltages of the source QD. Each point on the map shows the change in the current through the charge sensor (QPC) after sweeping the gates from a reference position to the gate values of that point and returning to the reference position. Each colour corresponds to a different number of electrons in the QD. The initial electron number before the sweep is zero ($N^{\text{init}} = 0$). The dotted line at $V_R^{\text{load}} = -0.70$ V marks the setpoint value for electron loading. **b**, Histogram of QPC currents from the map in **a**. **c**, Same map as in **a** but for an initial electron number $N^{\text{init}} = 3$. Dotted lines delimit the region (yellow) where the 3 electrons remain trapped in the dot. This map can be viewed as a holding map. **d**, Holding map for $N^{\text{init}} = 3$ in the gate range of the sending configuration.

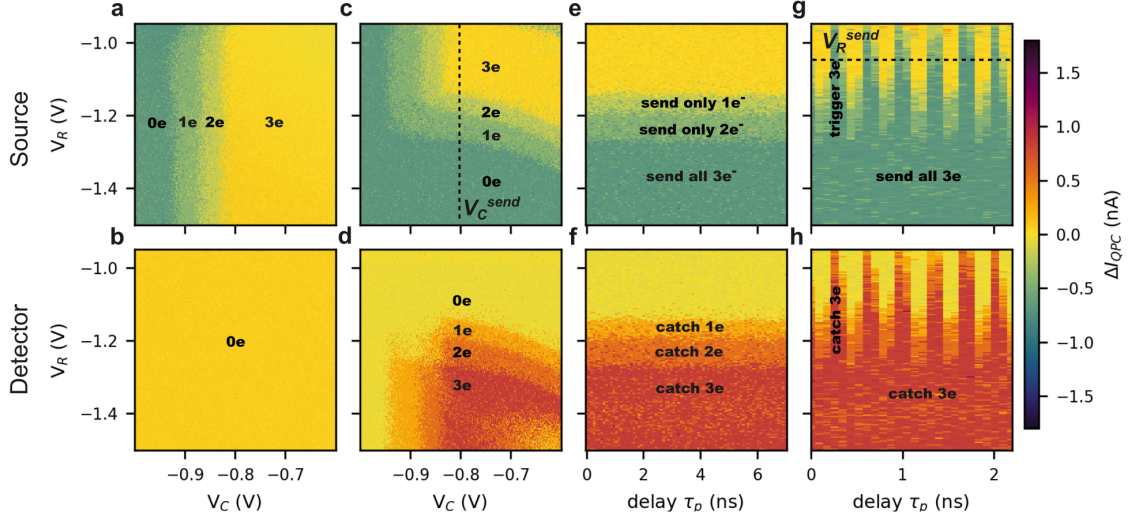


Fig. S2. **Controlled sending of $N = 3$ electrons.** Top panels: Sending maps of the source S1 starting. Bottom panels: Catching maps of the detector D2. The side gates of the central channel are adjusted to tilt the transverse potential well and direct all the electrons toward D2. Three electrons have been initially loaded into the source QD ($N^{init} = 3$). The voltage V_R is then set to a more negative value, to prevent electrons from escaping the dot towards the reservoir when the SAW arrives. **a,b**, Maps before applying the SAW, with all 3 electrons remaining in the source (yellow) and no electron in the detector (yellow). **c,d**, Maps after applying the SAW, showing that 1, 2, or 3 electrons are transferred from the source (green) to the detector (orange). **e,f**, Maps with the SAW applied, at a fixed voltage $V_C^{send} = -0.80$ V (working point for sending), recorded without trigger pulse in a control experiment to check the electron sending a function of V_R . **g,h**, Maps with the SAW applied, and with a trigger pulse applied on the plunger gate (P) at different time delays τ_P . Simultaneous sending of 3 electrons is achieved with a short negative pulse having $V_P = -0.50$ V and $\delta t_{trig} = T_{SAW}/4 \approx 90$ ps. The dotted line indicates the working point $V_R^{send} = -1.06$ V used to trigger the sending of 3 electrons.

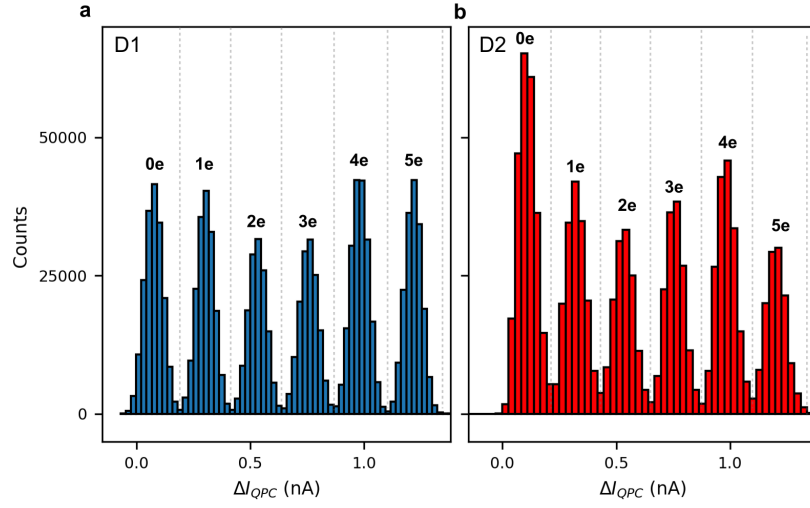


Fig. S3. **Multi-electron detection.** Histograms of the QPC current changes for (a) detector D1 and (b) detector D2, during the partitioning of $N = 5$ electrons within the same SAW minimum (data collected for a full sweep of side-gate detuning before post-selection of residual transfer errors). This illustrates the capability to detect up to five interacting electrons.

2. TUNING THE CENTRAL CHANNEL FOR $N = 1$ ELECTRON

In this section, we study the impact of the barrier-gate voltage V_B on single-electron ($N = 1$) partitioning at the Y-junction and estimate the effective electron temperature using a model for thermally-activated hopping in a double-well potential.

2.1. Experimental data

With side-gate voltages held constant around zero detuning to have symmetric partitioning, we measured the partitioning probability as function of the barrier-gate voltage V_B for a single electron sent from source S1 or from source S2 (Fig. S4a). At $V_B = -1.5$ V, the upper and lower rails are fully isolated, preventing electron from tunneling from one side to the other. For $V_B \geq -1.25$ V, electrons sent from sources S1 and S2 show the same partitioning result $P_{(0,1)} = P_{(1,0)}$ and hence are statistically indistinguishable. This property is the consequence of the very long ($40 \mu\text{m}$) central channel which gives the electron enough time to fully tunnel through the barrier. For all partitioning experiments reported in this work, the barrier-gate voltage has been fixed at $V_B^0 = -1.25$ V, such that both sources S1 and S2 can be used indifferently, with $P_{(N-n,n)}^{\text{S1}} = P_{(N-n,n)}^{\text{S2}} \equiv P_{(N-n,n)}$. In particular, the two synchronised sources are needed to inject more than 3 electrons in the central channel, since one source only cannot send more than 3 electrons with good transfer efficiency.

2.2. Double-well model

In the experiment, the electron droplet is confined in two dimensions by the combined influence of the *moving* piezoelectric potential induced by the SAW (longitudinal direction) and by the *electrostatic* potential induced by the surface gates (transverse direction). In the central channel, the presence of a narrow barrier gate in-between the two side gates introduces a small barrier in the middle of transverse confinement potential. The resulting double-well potential can be modelled by a simplified two-site system as discussed in Sec. 2.2.1 or calculated more accurately to extract quantitative parameters as explained in Sec. 2.2.2.

2.2.1. Two-site master-equation model

We model the the single-electron partitioning data with the two-site master equation

$$\partial_t \begin{pmatrix} P_U \\ P_L \end{pmatrix} = \begin{pmatrix} -\Gamma_{U \rightarrow L} & \Gamma_{L \rightarrow U} \\ \Gamma_{U \rightarrow L} & -\Gamma_{L \rightarrow U} \end{pmatrix} \begin{pmatrix} P_U \\ P_L \end{pmatrix}, \quad (\text{S.1})$$

where the time-independent transition rates $\Gamma_{U \rightarrow L}$ and $\Gamma_{L \rightarrow U}$ correspond to stochastic single-electron transitions from the upper to the lower rail (and vice-versa). Solving this system of coupled linear equations, two solutions for $P_U(t)$ are obtained corresponding to two different initial conditions: electron sent from S1 ($P_U^{\text{S1}}(0) = 1$) and electron sent from S2 ($P_U^{\text{S2}}(0) = 0$). The experimentally measured probabilities $P_{(0,1)}$ correspond to these solutions at $t = \tau$,

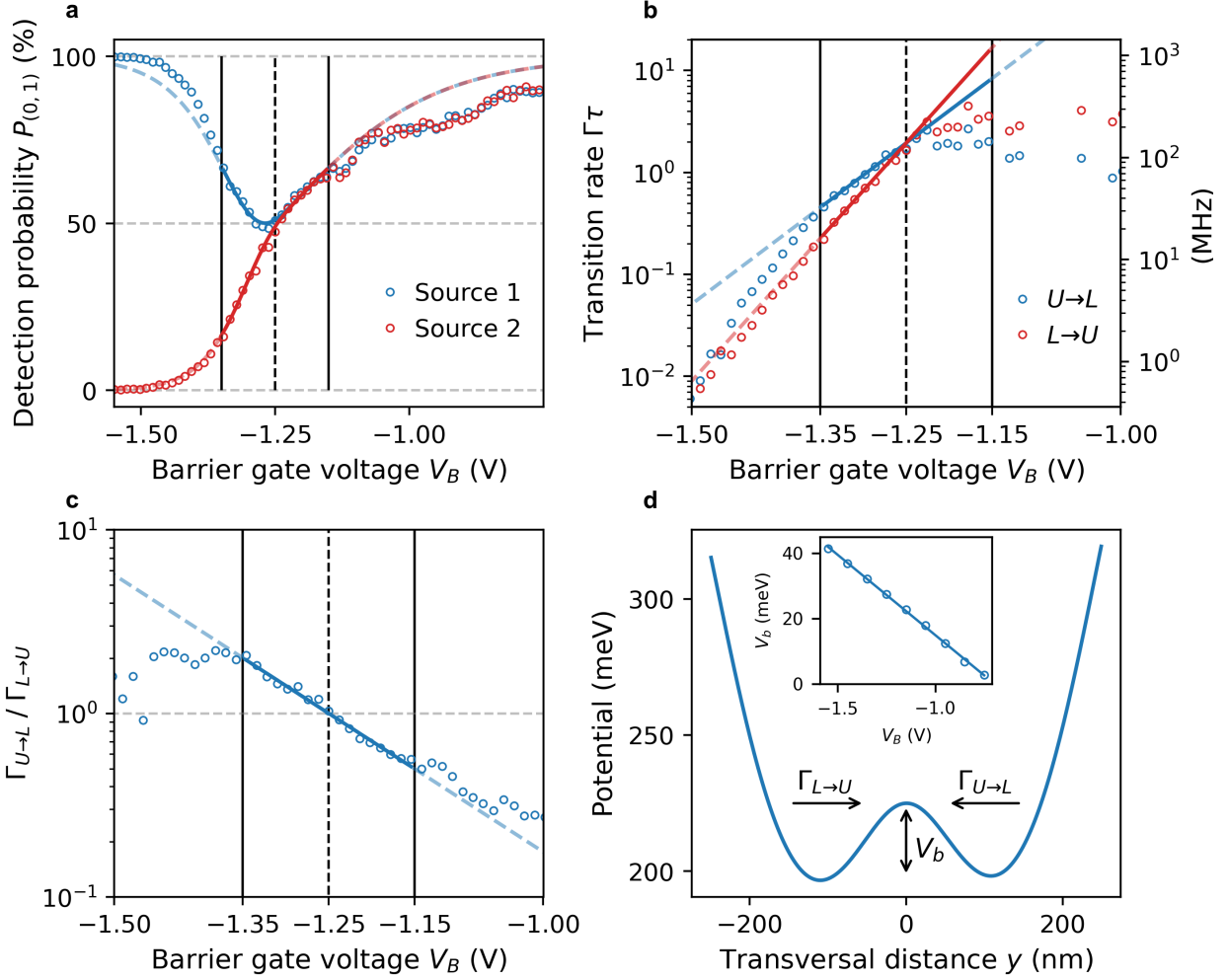


Fig. S4. **Tuning of the central channel.** **a**, Detection probabilities for single-electron partitioning as function of the barrier-gate voltage V_B and for fixed side-gate voltages $V_U = -1.108$ V and $V_L = -1.098$ V. The electron is sent either from the source S1 or from the source S2. Blue and red solid lines correspond to the two-site model fitted to the experimental data within the fit window around the working point at $V_B^0 = -1.25$ V, while dashed lines show the model outside the fit window (indicated by the vertical lines). **b**, Transition rates calculated from the experimentally measured detection probabilities after fitting with the two-site model. **c**, Ratio of transition rates for the two tunneling directions. **d**, Electrostatic simulation of the potential energy along the transverse direction. Inset shows barrier-height dependence on barrier-gate voltage.

where τ is the duration of the electron flight along the central channel,

$$\begin{aligned}
 P_U^{S1}(\tau) &= \frac{\Gamma_{L \rightarrow U} + \Gamma_{U \rightarrow L} e^{-(\Gamma_{U \rightarrow L} + \Gamma_{L \rightarrow U})\tau}}{\Gamma_{U \rightarrow L} + \Gamma_{L \rightarrow U}} \\
 P_U^{S2}(\tau) &= \frac{\Gamma_{L \rightarrow U} - \Gamma_{L \rightarrow U} e^{-(\Gamma_{U \rightarrow L} + \Gamma_{L \rightarrow U})\tau}}{\Gamma_{U \rightarrow L} + \Gamma_{L \rightarrow U}}
 \end{aligned} \tag{S.2}$$

By inverting these relations, the transition rates Γ can be expressed in terms of the

experimentally measured probabilities, as shown in Fig. S4b. In the vicinity of the working point selected for the partitioning experiments ($V_B^0 = -1.25$ V), the transition rates can be approximated as exponentially dependent on the barrier-gate voltage. For voltages above V_B^0 , the characteristic transition time $1/\Gamma$ is shorter than the duration of the flight in the central channel, giving rise to complete equilibrium between the two rails. The two electron exchange rates are not equal, and their ratio plotted in Fig. S4c is exponentially dependent on V_B .

Based on these observations, we express the rates as

$$\begin{aligned}\Gamma_{U \rightarrow L} &= \Gamma_0 e^{\alpha_B^{U \rightarrow L}(V_B - V_B^0)}, \\ \Gamma_{L \rightarrow U} &= \Gamma_0 e^{\alpha_B^{L \rightarrow U}(V_B - V_B^0)}.\end{aligned}\tag{S.3}$$

and fit the measured probabilities with the solutions (S.2) together with the expressions (S.3) as shown by solid lines in Fig. S4a. The model agrees well with experimental data within the fitting window and predicts qualitatively the measured probabilities outside the window. The best fit parameters are $\alpha_B^{U \rightarrow L} = 14.6$ V⁻¹, $\alpha_B^{L \rightarrow U} = 21.5$ V⁻¹ and $\Gamma_0 \tau = 1.94$.

2.2.2. Model for thermally activated hopping in a quartic double-well potential

We consider a simple 1D double well potential in form of a quartic polynomial, keeping the conventional notation [52],

$$V(y) = V_b + \mu_q \frac{y}{y_0} - 8V_b \frac{y^2}{y_0^2} + 16V_b \frac{y^4}{y_0^4}.\tag{S.4}$$

where V_b is the energy barrier and μ_q is the energy detuning. The potential has two minima at $y = \pm y_0/2$ which, for the sake of the estimates below, we identify with the two sites of the kinetic model considered in previous Sec. 2.2.1.

The theory of transition rates [53, 54] generically predicts two regimes that depend on the temperature $T = k_B/\beta$: tunneling for $T < T_0$ and hopping for $T > T_0$ where $T_0 = 3\hbar\omega_0/16$ is tunneling-to-hopping crossover temperature determined by the curvature of $V(y)$ near the top of the barrier between the two sites (at $y = 0$), $\omega_0 = \sqrt{32V_b/(my_0^2)}$ where $m = 0.067m_e$ for electrons in GaAs.

In the vicinity of the symmetric point and in the limit $\beta V_b \gg 1$, the temperature-dependent hopping rates can be approximated as

$$\begin{aligned}\Gamma_{U \rightarrow L} &= \Gamma_0^{(\text{cl})} e^{-\beta(V_b - \mu_q/2)}, \\ \Gamma_{L \rightarrow U} &= \Gamma_0^{(\text{cl})} e^{-\beta(V_b + \mu_q/2)},\end{aligned}\tag{S.5}$$

where the prefactor in the classical 1D limit [55] is $\Gamma_0^{(\text{cl})} = \omega_0/(2\pi)$.

We estimate the numerical values of the parameters of the quartic potential Eq. (S.4) using NextNano self-consistent 3D simulations of the electrostatic potential induced by the surface gates in the modulation-doped GaAs/AlGaAs heterostructure, including non-linear screening by the 2DEG in non-depleted regions. For the actual values of voltages applied to the side gates and barrier gate, the central channel is depleted and forms a double-well potential (Fig. S4d). The potential profile has been simulated for a range of experimental voltages V_B in the symmetric configuration $V_U = V_L$ (which implies $\mu_q = 0$). This allows us to estimate the lever-arm factor relating the experimental voltage V_B and the energy

barrier height V_b (energy difference between the central maximum and the lateral minima), as shown in the inset of Fig. S4d. The linear relation

$$V_b = c_1 V_B + c_0 \quad (\text{S.6})$$

provides the coefficients $c_1 = -49.2$ meV/V and $c_0 = -34.2$ meV. At the working point $V_B^0 = -1.25$ V, the barrier height is $V_b = 27.5$ meV. With $y_0 = 220$ nm, this gives a hopping rate $\omega_0 = 7$ THz and a tunneling-to-hopping crossover temperature $k_B T_0 = 0.85$ meV.

Since the barrier height V_b is linearly dependent on the barrier-gate voltage V_B through Eq. S.6, the exponents of the tunneling rates Γ in Eq. (S.5) can be compared with those of Eq. (S.3) to get the relation $\beta c_1 = \bar{\alpha}_B$ where the second term is the average of the two fitted coefficients. The effective electron temperature in the moving confinement potential is then obtained as

$$k_B T \equiv \beta^{-1} = \frac{2|c_1|}{\alpha_B^{U \rightarrow L} + \alpha_B^{L \rightarrow U}} = 2.73 \text{ meV}. \quad (\text{S.7})$$

The electrostatic simulations also provide the detuning lever-arm $\alpha = 0.2$ meV/mV, which can be used to get the effective electron temperature from the parameter $\beta\alpha = 0.062$ /mV of the data fitting with the Ising model, and we get $k_B T \equiv \beta^{-1} = 3.2$ meV in good agreement with the first value. Since $T \gg T_0$, this justifies our assumption that the experiment operates in the classical hopping regime.

One has to exercise caution in interpreting the above model estimates, since they only include single-electron hopping between two sites with a constant effective rate during the propagation time τ before reaching the Y-junction. Dynamics of electrons during partitioning at the Y-junction may additionally affect the freeze-out temperature assumed in the sudden quench model of multi-electron partitioning.

3. RECONSTRUCTION FORMULA FOR N INDEPENDENT ELECTRONS

Table S1 explain how to reconstruct the partitioning probabilities of $N \neq 1$ independent electrons from the knowledge of the $N = 1$ partitioning probabilities. This reconstruction is illustrated in Fig. S5.

e/e	$e/e/e$	$e/e/e/e$	$e/e/e/e/e$
$P_{(2,0)} = P_{(1,0)}^2$ $P_{(1,1)} = 2P_{(1,0)}P_{(0,1)}$ $P_{(0,2)} = P_{(0,1)}^2$	$P_{(3,0)} = P_{(1,0)}^3$ $P_{(2,1)} = 3P_{(1,0)}^2P_{(0,1)}$ $P_{(1,2)} = 3P_{(1,0)}P_{(0,1)}^2$ $P_{(0,3)} = P_{(0,1)}^3$	$P_{(4,0)} = P_{(1,0)}^4$ $P_{(3,1)} = 4P_{(1,0)}^3P_{(0,1)}$ $P_{(2,2)} = 6P_{(1,0)}^2P_{(0,1)}^2$ $P_{(1,3)} = 4P_{(1,0)}P_{(0,1)}^3$ $P_{(0,4)} = P_{(0,1)}^4$	$P_{(5,0)} = P_{(1,0)}^5$ $P_{(4,1)} = 5P_{(1,0)}^4P_{(0,1)}$ $P_{(3,2)} = 10P_{(1,0)}^3P_{(0,1)}^2$ $P_{(2,3)} = 10P_{(1,0)}^2P_{(0,1)}^3$ $P_{(1,4)} = 5P_{(1,0)}P_{(0,1)}^4$ $P_{(0,5)} = P_{(0,1)}^5$

Table S1. Expressions for reconstructing the partitioning probabilities $P_{(N-n,n)}$ of $N = 2, 3, 4,$ and 5 electrons in different SAW minima (non-interacting), using the experimental partitioning probabilities $P_{(1,0)}$ and $P_{(0,1)}$ of a single electron ($N = 1$), as illustrated in Fig. S5.

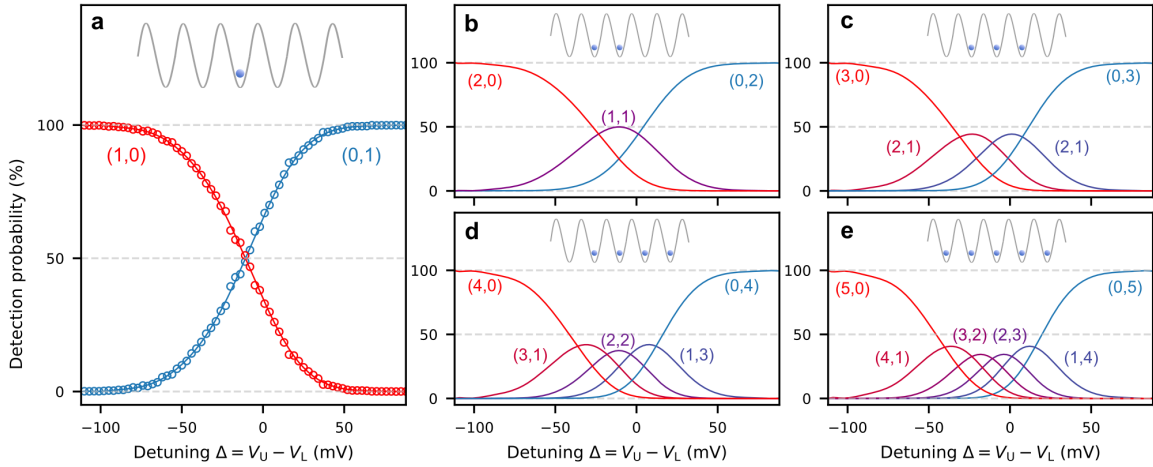


Fig. S5. **Reconstruction of partitioning probabilities of uncorrelated electrons using single-electron data.** **a** Probability distributions for single-electron partitioning as function of side-gates detuning, for $V_B = -1.25$ V. Each data point is based on 3,000 single-shot measurements. Solid lines are 15th-order polynomial fits, which are used to model multi-electron partitioning probabilities corresponding to uncorrelated electrons distributed among different SAW minima. **b-e**, Reconstruction of the partitioning probabilities for $N = 2, 3, 4,$ and 5 uncorrelated electrons placed in different SAW minima, using the expressions given in Table S1.

4. COUNTING STATISTICS AND CUMULANTS

4.1. Multivariate and univariate cumulants

The outcome of the partitioning experiment can be represented by the probabilities p_n to detect n electrons at a chosen detector (here D1), as done in full counting statistics (FCS) [56]. This probability distribution can be characterised in terms of either moments $\langle n^k \rangle$ or cumulants $\langle\langle n^k \rangle\rangle$, which are related to each other by the formal expansion of the appropriate generating function

$$\ln \langle e^{zn} \rangle = \ln \left(\sum_{k=0}^{\infty} \langle n^k \rangle z^k / k! \right) = \sum_{k=1}^{\infty} \langle\langle n^k \rangle\rangle z^k / k! \quad (\text{S.8})$$

where $\langle f(n) \rangle = \sum_n p_n f(n)$ denotes averaging over the probabilities of the FCS. One can express moments through cumulants

$$\langle n^k \rangle = \sum_{j=0}^k B_{kj} (\langle\langle n \rangle\rangle, \langle\langle n^2 \rangle\rangle, \dots, \langle\langle n^j \rangle\rangle) \quad (\text{S.9})$$

and vice versa

$$\langle\langle n^k \rangle\rangle = \sum_{j=1}^k (j-1)! (-1)^{j-1} B_{kj} (\langle n \rangle, \langle n^2 \rangle, \dots, \langle n^{k-j+1} \rangle) \quad (\text{S.10})$$

where B_{kj} are the partial Bell polynomials [46].

Two properties of regular (univariate) cumulants are noteworthy in the context of studying correlations between partitioning events, for an ensemble of N particles. Firstly, that they are additive for independent variables. In our case, the number n of particles detected at D1 can be written as the sum $n = \sum_{j=1}^N T_j$ of binary variables $T_j \in \{0, 1\}$ coding the absence (0) or presence (1) of the particle j in the detector D1 for a given realization of the partitioning experiment. If the variables T_j are statistically independent (p_n following a binomial distribution), then $\langle\langle n^k \rangle\rangle_N = N \langle\langle n^k \rangle\rangle_1$. Secondly, if p_n follows Gaussian distribution, $\langle\langle n^k \rangle\rangle = 0$ if $k > 2$. Note that this property is valid only for continuous n , so higher-order ($k > 2$) non-zero cumulants serve as an indication of deviations from Gaussian behaviour but do not distinguish between the effects of discrete n and correlations induced by interactions.

The univariate cumulants $\langle\langle n^k \rangle\rangle$ discussed above are therefore not good indicators of interparticle correlations, as they remain nonzero even when the partitioning is independent. Instead, we consider multivariate cumulants $\langle\langle T_1^{i_1} \dots T_N^{i_N} \rangle\rangle$ defined with a generating function

$$\ln \langle e^{\mathbf{z} \cdot \mathbf{T}} \rangle = \sum_{i_1, i_2, \dots, i_N} \langle\langle T_1^{i_1} \dots T_N^{i_N} \rangle\rangle \frac{z_1^{i_1} \dots z_N^{i_N}}{i_1! \dots i_N!} \quad (\text{S.11})$$

where $\mathbf{T} = (T_1, \dots, T_N)$ and $\mathbf{z} = (z_1, \dots, z_N)$. The sum $i_1 + i_2 + \dots + i_N = k$ counts the number of variables T_j (including possible repetitions) involved in the cumulant and represents the order of the cumulant. For a given k , there is one multivariate cumulant for each $\{i_1, \dots, i_N\}$ leading to a large number of non-equivalent multivariate cumulants if the variables are not equivalent.

Multivariate cumulants carry more information than univariate cumulants because they

capture correlations between multiple variables, allowing for the analysis of many-body systems with correlations between several particles. The key advantage is that a multivariate cumulant between two independent variables T_a and T_b is zero, hence higher-order cumulants reveal the presence of multi-body correlations. In statistics, the multivariate cumulants [35] are also referred to as irreducible correlators, and in field theory, they are known as connected diagrams or connected correlators. Multivariate cumulants and moments are related by general formulas; this relationship is a combinatorial procedure that involves summing over all possible partitions of the indices corresponding to the order k of the cumulant [47]. A more detailed example of applying the general formulas for specific symmetry (determined by electron configuration in SAW minima) is provided in Supplementary note 5).

4.2. Relation between symmetrised multivariate cumulants and univariate full counting statistics

FCS measures the cumulative observable $n = \sum_j T_j$ which is symmetric under the permutation of particles. Here we show that knowing the FCS is equivalent to knowledge of all symmetrised multivariate moments m_k , Eq. (2) in Methods. For permutation-symmetric distributions, any multivariate moment or cumulant of k distinct variables depends only on k , hence in the fully symmetric case, the knowledge of m_k implies the knowledge of the corresponding multivariate cumulants κ_k , which can therefore be calculated from the probabilities p_n of the FCS.

We define the fully symmetrised k -th order multivariate moments m_k as an average over all distinct combinations of k variables out of N

$$m_k = \binom{N}{k}^{-1} \langle e_k(T_1, \dots, T_N) \rangle \quad (\text{S.12})$$

where $\binom{N}{k} = \frac{N!}{k!(N-k)!}$ is the binomial coefficient and

$$e_k(T_1, \dots, T_N) = \sum_{1 \leq j_1 < j_2 < \dots < j_k \leq N} T_{j_1} T_{j_2} \dots T_{j_k} \quad (\text{S.13})$$

is the elementary symmetric polynomial in the N variables T_1, \dots, T_N , which is made of $\binom{N}{k}$ terms corresponding to all possible combinations of k variables T_j out of N .

Since $T_{j_1} T_{j_2} \dots T_{j_k}$ equals to 1 if and only if the subset $\{j_1, j_2, \dots, j_k\}$ of k variables is among the ensemble of particles detected in D1, the quantity $\langle e_k(T_1, \dots, T_N) \rangle$ is the sum of all the probabilities p_n with $n \geq k$ multiplied by the number $\binom{n}{k}$ of possibilities to take k terms out of n . In terms of FCS, the symmetrised multivariate moments can therefore be written

$$m_k = \binom{N}{k}^{-1} \sum_{n=k}^N \binom{n}{k} p_n. \quad (\text{S.14})$$

This result can be mathematically demonstrated as follows. In our case, the variables T_j are binary ($T_j \in \mathbb{Z}^2$) and idempotent ($T_j^2 = T_j$). Under these conditions, a multiplication law $e_1 e_j = j e_j + (j+1) e_{j+1}$ holds true. Using this multiplication law, one can prove the identity $\binom{e_1}{k} = e_k$ by induction. As $e_1 = \sum_{j=1}^N T_j = n$, the elementary symmetric polynomial e_k is simply equal to the binomial coefficient $\binom{n}{k}$ and the symmetrised multivariate moment

(S.12) writes

$$m_k = \binom{N}{k}^{-1} \left\langle \binom{n}{k} \right\rangle = \binom{N}{k}^{-1} \sum_{n=k}^N \binom{n}{k} p_n \quad (\text{S.15})$$

as anticipated above, or equivalently

$$m_k = \frac{\langle (n)_k \rangle}{(N)_k} \quad (\text{S.16})$$

where $(n)_k = n(n-1)\dots(n-k+1)$ is the falling factorial and $\langle (n)_k \rangle$ is called the factorial moment of order k .

Similar to (S.12) we define the symmetrised k -th order multivariate cumulants

$$\kappa_k = \binom{N}{k}^{-1} \langle\langle e_k(T_1 \dots T_N) \rangle\rangle. \quad (\text{S.17})$$

When the system is fully symmetric under permutations, all multivariate moments and cumulants of k -th order are the same and equal to $m_k = \langle T_1 T_2 \dots T_k \rangle$ and $\kappa_k = \langle\langle T_1 T_2 \dots T_k \rangle\rangle$. In this case of full statistical equivalence between the particles, the relation between the symmetric multivariate moments m_k and cumulants κ_k are exactly the same as between the regular univariate moments $\langle n^k \rangle$ and cumulants $\langle\langle n^k \rangle\rangle$. Hence the standard combinatorial formula Eq. (S.10) applies

$$\kappa_k = \sum_{j=1}^k (j-1)! (-1)^{j-1} B_{kj} \left(\frac{\langle n \rangle}{N}, \frac{\langle (n)_2 \rangle}{(N)_2}, \dots, \frac{\langle (n)_{k-j+1} \rangle}{(N)_{k-j+1}} \right) \quad (\text{S.18})$$

where B_{kj} are the partial Bell polynomials. For reference, we quote the explicit relations for the values of k involved in the experiment

$$\kappa_1 = m_1 \quad (\text{S.19a})$$

$$\kappa_2 = -m_1^2 + m_2 \quad (\text{S.19b})$$

$$\kappa_3 = 2m_1^3 - 3m_2 m_1 + m_3 \quad (\text{S.19c})$$

$$\kappa_4 = -6m_1^4 + 12m_1^2 m_2 - 4m_1 m_3 - 3m_2^2 + m_4 \quad (\text{S.19d})$$

$$\kappa_5 = 24m_1^5 - 60m_1^3 m_2 - 5m_1 m_4 - 10m_2 m_3 + 20m_1^2 m_3 + 30m_1 m_2^2 + m_5 \quad (\text{S.19e})$$

Together with (S.14) these relations are used to compute symmetrised multivariate cumulants from the experimental counting statistics $p_n = P_{(N-n, n)}$.

4.3. Comparison of different types of cumulants for FCS

One can also define factorial cumulants [29, 48] $\langle\langle n^k \rangle\rangle_F$, whose generating function is $\ln \langle e^{zn} \rangle = \sum_{k=1}^{\infty} \langle\langle n^k \rangle\rangle_F (z-1)^k / k!$ (expansion of the univariate cumulant generating function around $z=1$). The corresponding factorial moments are $\langle (n)_k \rangle = \langle n(n-1)\dots(n-k+1) \rangle$ [48] and the relations between factorial moments $\langle (n)_k \rangle$ and cumulants $\langle\langle n^k \rangle\rangle_F$ are the same as between univariate moments and cumulants in Eq. (S.9) and Eq. (S.10). The advantage of factorial cumulants is evident in a Poisson distribution, where all $\langle\langle n^k \rangle\rangle_F = 0$ for $k > 1$.

We note that κ_k is *not* a factorial cumulant of the FCS because of the factor $(N)_k$ in

the relation (S.16) between the symmetrised multivariate moment m_k and FCS factorial moment $\langle(n)_k\rangle$.

The difference between regular univariate cumulants $\langle\langle n^k \rangle\rangle$, factorial cumulants $\langle\langle n^k \rangle\rangle_F$ and the symmetric partitioning multivariate cumulants κ_k can also be understood in terms of reference probability distributions. Namely, $\langle\langle n^k \rangle\rangle = 0$, $\langle\langle n^k \rangle\rangle_F = 0$ and $\kappa_k = 0$ for $k \geq 2$ for Gaussian (in continuous n limit), Poisson and binomial distributions, respectively.

5. ANALYSIS OF 2E/2E ($N = 4$) PARTITIONING DATA

To explore a less symmetric configuration with non-equivalent same-order cumulants, four electrons are sent ($N = 4$) such that the electrons are placed in pairs in two adjacent SAW minima (configuration denoted as 2e/2e). Similar to the case of one electron per minimum analysed in Fig. 2a, we can check from the counting statistics that electrons in different SAW minima remain uncorrelated. This is done by reconstructing the partitioning probabilities for the 2e/2e case from the experimental partitioning data where only one minimum is filled with two electrons (case 2e, $N = 2$), using the convolution of corresponding probability distributions

$$\begin{aligned}
 P_{(4,0)} &= P_{(2,0)}^2 \\
 P_{(3,1)} &= 2P_{(1,1)}P_{(2,0)} \\
 P_{(2,2)} &= P_{(1,1)}^2 + P_{(2,0)}P_{(0,2)} \\
 P_{(1,3)} &= 2P_{(1,1)}P_{(0,2)} \\
 P_{(0,4)} &= P_{(0,2)}^2.
 \end{aligned}
 \tag{S.20}$$

The measured and reconstructed probabilities are shown in Fig. S6 and are in good agreement, confirming the absence of inter-SAW minima correlations.

Further, we use this 2e/2e case (with interactions restricted to the electron pairs occupying the same minimum) to illustrate how higher-order multivariate cumulants can be calculated in case of partial permutational symmetry. The general formulas [47] expressing the relations between the multivariate moments $\langle T_{j_1}^{i_1} T_{j_2}^{i_2} \dots T_{j_l}^{i_l} \rangle$ and the multivariate cumulants can be summarised as follows [50]

$$\langle\langle T_{j_1}^{i_1} \dots T_{j_l}^{i_l} \rangle\rangle = \sum_{\{\mathcal{P}_l\}} (|\mathcal{P}_l| - 1)! (-1)^{|\mathcal{P}_l| - 1} \sum_{B \in \mathcal{P}_l} \left\langle \prod_{r \in B} T_{j_r}^{i_r} \right\rangle,
 \tag{S.21}$$

where $\{\mathcal{P}_l\}$ denotes the list of all partitions of a set $\{1, 2, \dots, l\}$ for a total of l variables. $B \in \mathcal{P}_l$ is a block in a partition \mathcal{P}_l , and $|\mathcal{P}_l|$ counts the number of blocks in that partition. In our case, we only consider cumulants $\langle\langle T_{j_1} T_{j_2} \dots T_{j_l} \rangle\rangle$ as the variables are idempotent ($T_j^2 = T_j$).

While general formulas are always valid, they involve too many different cumulants $\langle\langle T_{j_1} T_{j_2} \dots T_{j_l} \rangle\rangle$ for all to be determined by the partitioning data. However, symmetry considerations may lead to significant reduction in the number of non-equivalent multivariate functions. For complete permutational symmetry (when all electrons are statistically indistinguishable, e.g., all placed either in different or in the same SAW minimum), the cumulants κ_k are completely determined by counting statistics p_n , as described in Methods and Supplementary note 4. In particular, Eq. (S.21) leads to Eq. (S.18) with Eq. (S.16) in this case. For systems that are not fully symmetric under permutations, not all multivariate cumulants of k -th order are equal in general and Eq. (S.18) for calculating the symmetrised cumulants κ_k from the symmetrised moments m_k is no longer applicable (however, the cumulants κ_k are always defined as (S.17)).

Here we examine a specific case with partial symmetry which follows from considering the particular placement of the electrons in the SAW minima. In the present example of 2e/2e electrons, placing 2 electrons in adjacent SAW minima will lead to different interaction strengths between electrons in the same minimum compared to those in separate ones. We index electrons such that $\{1, 2\}$ corresponds to the pair in one minimum (denoted with \bullet) and

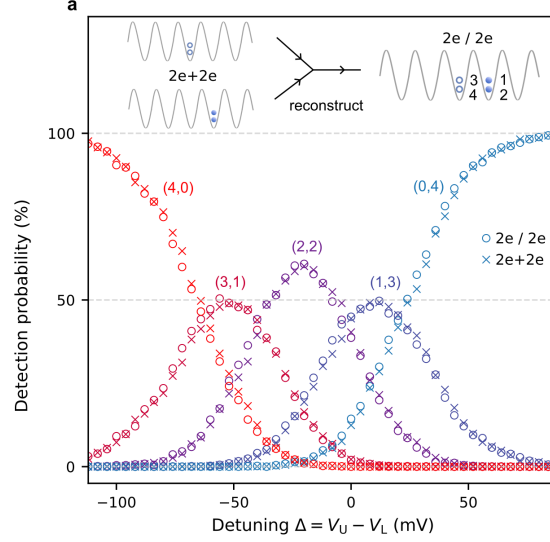


Fig. S6. **Experimental reconstruction of $2e/2e$ ($N = 4$) from $2e$ ($N = 2$).** Detection probabilities for the partitioning of four electrons in a configuration with two electrons in each of two adjacent minima ($2e/2e$) compared to its reconstruction calculated from the detection probabilities measured from the partitioning of two interacting electrons in a single minimum ($2e$) using Eq. (S.20). Each data point is obtained from 3,000 single-shot measurements.

$\{3,4\}$ to the other pair (denoted with \circ). There are only two non-equivalent second-order multivariate cumulants, one for electrons in the same minimum $\langle\langle T_1 T_2 \rangle\rangle = \langle\langle T_3 T_4 \rangle\rangle = \langle\langle \bullet \bullet \rangle\rangle$ and one for electrons in different minima $\langle\langle T_1 T_3 \rangle\rangle = \langle\langle T_1 T_4 \rangle\rangle = \langle\langle T_2 T_3 \rangle\rangle = \langle\langle T_2 T_4 \rangle\rangle = \langle\langle \bullet \circ \rangle\rangle$. Hence, following the definition (S.17), κ_2 is expressed as $\kappa_2 = (2\langle\langle \bullet \bullet \rangle\rangle + 4\langle\langle \bullet \circ \rangle\rangle) / 6$. The third-order multivariate cumulants $\langle\langle T_a T_b T_c \rangle\rangle = \langle\langle \bullet \bullet \circ \rangle\rangle = \langle\langle \bullet \circ \circ \rangle\rangle = \kappa_3$ are all equal, as the subsystem remains physically equivalent for selection of any subset of three electrons (two electrons in the same minimum and one in another). Therefore, symmetrised κ_3 can be used for any third-order cumulant in Eq. (S.21).

Using the above partial symmetry conditions and Eq. (S.14), (S.21), we express partitioning probabilities p_n via multivariate cumulants (Table S2). With two different second-order cumulants, the system is undetermined. However, based on the reconstruction of $2e/2e$ ($N = 4$) probability distribution from $2e$ ($N = 2$) partitioning data, we have confirmed that there is no inter-SAW-minima correlation, $\langle\langle \bullet \circ \rangle\rangle = 0$. This condition allows us to compute the cumulants using the expressions in Table S2 by setting $\langle\langle \bullet \circ \rangle\rangle = 0$. In this case $\kappa_2 = \langle\langle \bullet \bullet \rangle\rangle / 3$. The symmetrised cumulants κ_2 , κ_3 and κ_4 computed in this way are depicted in Fig. 2e of the main text. One can see that κ_3 and κ_4 are close to zero, demonstrating the absence of higher than second-order correlations.

Alternatively, we could have assumed that $\kappa_4 = 0$ and then computed $\langle\langle \bullet \bullet \rangle\rangle$ and $\langle\langle \bullet \circ \rangle\rangle$ separately (with the expectation that the latter will be close to zero).

p_n	κ_1	κ_1^2	κ_1^3	κ_1^4	$\langle\langle\bullet\bullet\rangle\rangle$	$\langle\langle\bullet\circ\rangle\rangle$	$\kappa_1\langle\langle\bullet\bullet\rangle\rangle$	$\kappa_1\langle\langle\bullet\circ\rangle\rangle$	$\kappa_1^2\langle\langle\bullet\bullet\rangle\rangle$	$\kappa_1^2\langle\langle\bullet\circ\rangle\rangle$	$\langle\langle\bullet\bullet\rangle\rangle^2$	$\langle\langle\bullet\circ\rangle\rangle^2$	κ_3	$\kappa_1\kappa_3$	κ_4	1
p_0	-4	6	-4	1	2	4	-4	-8	2	4	1	2	-4	4	1	1
p_1	4	-12	12	-4	-4	-8	12	24	-8	-16	-4	-8	12	-16	-4	0
p_2	0	6	-12	6	2	4	-12	-24	12	24	6	12	-12	24	6	0
p_3	0	0	4	-4	0	0	4	8	-8	-16	-4	-8	4	-16	-4	0
p_4	0	0	0	1	0	0	0	0	2	4	1	2	0	4	1	0

Table S2. **Probabilities and cumulants for the 2e/2e ($N = 4$) case.** Coefficients for expressing the probabilities $p_n = P_{(N-n, n)}$ from the multivariate cumulants, taking into account the symmetry but without assumption about the strength of the intra-minimum versus inter-minimum interaction. p_n is the sum of the terms in the top row with each term multiplied by its corresponding coefficient.